CONCURRENT SIMULATION OF A SUBJECT SPECIFIC MUSCULOSKELETAL MODEL WITH ANATOMICAL KNEE

A Thesis

presented to

the Faculty of the Graduate School

at the University of Missouri-Columbia

In Partial Fulfillment

of the Requirements for the Degree

Master of Science

---

by

HAMIDREZA JAHANDAR

Dr. TRENT GUESS, Thesis Supervisor

JULY 2015

The undersigned, appointed by the dean of the Graduate School, have examined the thesis entitled

Concurrent Simulation of a Subject Specific

Musculoskeletal Model with Anatomical Knee

presented by Hamidreza Jahandar,

a candidate for the degree of master of science,

and hereby certify that, in their opinion, it is worthy of acceptance.

Dr. Trent Guess, Associate Professor
Department of Physical Therapy and Orthopaedic Surgery

Dr. Sheila Grant , Professor
Department of Bioengineering

Dr. Stephen Sayers, Associate Professor
Department of Physical Therapy

Dr. Ferris Pfeiffer , Assistant Professor
Department of Bioengineering

This should go to my parents who gave me so much and continue to support me throughout my life every day.

ACKNOWLEDGEMENTS

First of all, I would like to thank Dr. Guess for the greatest three years of my life. Working for Dr. Guess is one of the best things that have happened in my life. I also would like to thank Mr. (soon to be Dr.) Swithin Razu and Dr. Antonis Stylianou for their insight throughout this project. The faculty and staff at Department of Physical therapy provided the greatest atmosphere for me to do my research. And last but not least I would like to thank my cousin, Dr. Mohamad Kia who introduced me to the field of biomechanics.

Table of Contents

List of Figures

List of Tables

CONCURRENT SIMULATION OF A SUBJECT SPECIFIC MUSCOLUSKELETAL MODEL WITH ANATOMICAL KNEE

Hamidreza Jahandar

Dr. Trent Guess, Thesis Supervisor

ABSTRACT

Computational models of the knee provide us with a better understanding of ligament and joint contact forces during ambulatory activities. Thus, such models can be used to devise better injury prevention methods, as well as surgical and therapeutic treatments for musculoskeletal disorders. This manuscript presents a method to develop a subject specific model in a multi-body framework. The muscle-driven computational model is created by segmenting the magnetic resonance imaging data and uses motion capture data to predict the knee mechanics in gait. The model is validated against the ground reaction forces and then is used to examine the laxity of the knee, the function of menisci as well as pressure distribution in the patellofemoral joint.

Chapter 1

Introduction

Biomechanics (the science of analyzing the mechanics of biological systems) provides useful insight to current global healthcare issues such as cardiovascular problems and musculoskeletal disorders (MSDs). Cardiovascular diseases and stroke account for 1 in 4 deaths in US (CDC Wonder Online Database) and account for more than $312.6 billion in cost (AHA Statistical Update 2014). MSDs such as Osteoarthritis (OA) – a joint disease that deteriorates the articular cartilage - reduce the quality of life and are estimated to cost a total of $125 billion per year [Gallagher et al. 2013]. OA accounts for a considerable portion of this cost. Lawrence et al. (2008) estimated that 13.9% of adults aged 25 year and older are affected by OA, and it results in a $28.5 billion and $13.7 billion for total knee and hip joint replacements respectively per year [Murphy and Helmick 2012].

Rigid Body Dynamics, Solid Mechanics and Fluid Mechanics are the three main mechanical engineering principles that are used to answer research questions in the fields of Musculoskeletal Systems, Tissue deformities and Cardiovascular Systems respectively. Cardiovascular systems are beyond the scope of this manuscript and will not be discussed any further (The field is discussed in detail by Chandran K.B.).

Numerous treatments of musculoskeletal disorders consider the joint as an organ and not as a collection of individual independent tissues. The interaction of tissues with each other in every organ, play an important role in the well-being of the whole organ. Any change to even one of the tissues might jeopardize a healthy joint. A follow up study on 1337 John Hopkins medical students (91% male, 91% white and mean age 22 years)

reported an increased risk of developing OA significantly following a joint injury (relative risk of 5.17) [Gelbar et al. 2000]. Abnormal joint pressure is regarded as one of the common pathways leading to degenerative joint diseases such as OA. Therefore, the mechanical environment in the joint and any disturbance of it (either by impact injuries or musculoskeletal disorders) has been the subject of many studies.

For example meniscal tears and the subsequent meniscal surgery is believed to be one of the established risk factor in the onset of OA in the knee. Out of the 155 patients (mean age = 54 years old) who had undergone partial meniscectomy surgery with no other injury, 43 percent had radiographic features of osteoarthritis while 59% of those were symptomatic after 16 years [Englund et al. 2003]. Conservative treatments are usually considered for patients with less physically demanding life styles. However, conservative treatments have been shown to be ineffective in response to joint injuries such as anterior cruciate ligament (ACL) ruptures. Out of the 73 patients with acute ACL ruptures classified suitable for primarily conservative treatment after a preoperative screening, only one third show a good or very good result [Strehl A and Eggli, 2007].

The notion of treating the joint as a whole organ, not as individual tissues, has resulted in elimination of invasive surgeries such as meniscectomy (complete removal of injured menisci). A study on the late effects of meniscectomy ten to thirty years after surgery revealed that only 10 percent of women who underwent the surgery had symptom-free knees [Tapper et. al, 1969]. Less invasive methods such as arthroscopic surgeries have been introduced to preserve the joint capsule as much as possible and have provided satisfactory results. For instance, central quadriceps tendon-bone autograft performed on patients with ACL injuries produced successful results in a majority of

patients 27 to 49 months post operatively [Lee et. al, 2004]. Therefore, the complicated interaction of tissues inside the knee plays a crucial role in the well-being of the organ. Thorough understanding of this complex interaction enables the healthcare professionals to design better treatment plans and also provide better injury prevention methods.

Injuries and chronic musculoskeletal problems often lead to abnormal joint kinematics and kinetics. Therefore, the best outcome of a treatment plan is restoring the joint kinematics and kinetics. However, the normal kinematics and kinetics of the joint is not completely understood. Therefore, the surgical interventions to restore the joint to the initial condition are limited. Information about internal mechanics of the joints as well as forces exerted by the muscles during ambulatory activities can help solve this problem.

Experimental studies, both in-vitro (experiment performed outside the normal biological context) cadaveric studies and in-vivo (experiments within the living organism) gait measurements, have provided insight into musculoskeletal disorders and also the interactions of the nervous and musculoskeletal systems of the body, interactions that result in coordinated motion of body segments relative to each other.

Cadaver experiments are used for different purposes; for example, measuring material properties of soft tissue, studying the mechanical response of the joint to specific loading conditions and also serving as a validation tool for computational studies. For instance, industrial six-degree of freedom robots matched with a universal force-moment sensor (UFS) have been used recently to calculate the internal forces of the joint in addition to measuring accurate kinematics in the 3-D envelope of motion. One example was the Kawasaki ZX165U matched with a Delta UFS (ATI). Heyse et al. (2015) analyzed the ability of Unicondylar Knee Arthroplasty (UKA) to restore the kinematics of the knee

both in Balanced (normal installation of the implant) and Overstuffed (thicker inlay of polyethylene in the medial compartment) implant. The kinematics was measured in response to axial loading of 200 N in addition to a 15 Nm Abduction moment. Another example of utilizing an industrial robot matched with a UFS was presented by Kanamori et al. (2000). A Puma robot model 762 (Unimate, Pittsburgh, PA) was matched with model 4015 UFS (JR3 Inc, Woodland, CA) in order to compare the kinematics of intact and anterior cruciate ligament (ACL) deficient knee in response to tibial torque of 10 Nm and pivot shift test (a combination of 10 Nm internal tibial torque and 10 Nm Valgus). Moreover, the ACL force was calculated at specific knee angles by serial sectioning method, a method in which the force taken by a constraint (ACL in this case) is measured by comparing the loading applied by the robotic arm before and after dissection, when the knee is in that specific spot. Mechanical testing equipment has also been used to explore the joint kinematics and kinetics in only one or two degrees of freedom. For example Senavongse and Amis (2005) used an Instron 1122 materials testing machine (Instron Ltd., Massachusetts, US) to analyze the medial-lateral stability of the patella after injury on eight cadaver knees.

Another avenue in experimental biomechanics is gait analysis. Motion capture systems track the position and orientation of body segments while force plates determine the direction and magnitude of the resultant ground reaction force and surface electromyography (EMG) electrodes as well as indwelling EMG sensors record the activation of muscles. Indwelling EMG electrodes such as quadrifilar needle sensors and quadrilfilar wire sensors have been used in the past (De Luca et. al, 1972) to record EMG signals from individual muscles. Due to the fact that they are inserted into the muscle,

indwelling electrodes do not record any cross talk providing a more accurate activation signal. Moreover, indwelling electrodes have access to muscles in deeper layers of the body. Surface EMG electrodes provide a better indication of overall muscle activation, thus, surface EMG electrodes are mainly used in the field musculoskeletal biomechanics.

Gait analysis can be used to evaluate athletic performance in addition to analyzing injury probability among other applications. Gait measurements provide useful information on the moments acting about the joint and also ground reaction forces, but they are inadequate when it comes to internal loading of the joints and mechanical interactions of the joint's tissues. Hewett et al. (2004) used an Eagle camera system (Motion Analysis) combined with force measurement from AMTI force plates to determine that increased valgus moment and valgus motion of the knee at the impact phase of landing are key predictors of an increased potential for ACL injury.

Experimental studies provide valuable insight into the kinetics and kinematics of the joint. However, there are so many limitations to these types of experiments. Cadaveric studies mostly use old subjects and there is no data on whether old cadavers and young cadavers have the same mechanical characteristics [Couppé C et. al, 2009]. Thus, application of the results in clinical settings is under question. Moreover, muscle forces, which play an important role in stability and load distribution of the joints, cannot be utilized. In gait analysis, joint torques are calculated by modeling the human joints as simplified engineering joints, for example, the hip is modeled as a ball and socket joint. Joint torques provides useful information especially in injury prevention and athletic training. However the results do not provide information about the internal mechanics of the joint such as ligament forces and contact pressure. Another downside of experimental

analysis is the expensive cost of the equipment and also availability of the subjects. Moreover, experimental methods are prone to operator errors and equipment malfunction. For instance, in cadaveric studies, a malfunctioning digitizer might threaten the integrity of the data. Furthermore, quantities such as tissue deformation are almost impossible to measure in-vivo and in-vitro.

In-silico methods (using computational models to conduct a biological experiment) in contrast to experimental methods are capable of examining the loading environment of the joint. Computational models will be helpful in understanding the mechanical interaction of tissues within a joint and enables researchers to answer the questions that are not possible in the real world. Most importantly, computational models can answer "What if" scenarios easily by modifying a few parameters. Due to the complex non-linear nature of soft tissues material properties (anisotropy, inhomogeneity and viscoelasticity), computational methods are widely used to study the function and structure of soft tissues. For example Lai et al. (2015) developed a Finite Element (FE) technique (a computational method that finds approximate solution to a partial differential equations system) to study knee laxity. Nine anatomical knees were modeled using the femoral and tibial cartilage, menisci, cruciate and collateral ligaments. The only difference between the models was the stiffness of the PCL. Posterior translation of the tibia was examined in result of a 100 N posterior tibial drawer load.

FE provides detailed data into the mechanical environment of biological tissue. For example, strain within tissue can only be studied using FE methods. However, FE models are computationally intensive and are usually used to analyze specific loading conditions that result in small deformations or vice versa. For instance, Kiapour et al. (2014)

predicted the contact mechanics and kinematics of an anatomical knee in response to only four simple quasi-static loading profiles. Thus, FE models typically only analyze a small portion of the 3-D envelope of motion and understanding of joint mechanics in a dynamic situation is not feasible. Moreover, concurrent simulation of a musculoskeletal model to calculate the muscle forces and joint contact forces simultaneously is not practical.

In contrast to FE models, rigid multi-body dynamics modeling (modeling the systems as a group of interconnected rigid bodies, which may undergo significant translation and rotational motion relative to each other) provides a system of equations that is noticeably less computationally intensive and requires considerably less time to solve. Therefore, the method enables researchers to examine more complex models both in terms of structure and boundary conditions. Simulating ambulatory activities is possible in multi-body environment with the current state of processing technology available to the public. But, modeling the full range of motion of the knee in the finite element method requires a considerable computational effort as well as oversimplification of the boundary loading condition [Shim et al. 2015].

For example, Shelburne et al. (2006) developed a computational model of the leg in the rigid body environment to predict knee contact force. They used a dynamic optimization solution of normal walking to calculate ground reaction force, joint angle and muscle forces.

Rigid multi-body modeling is an efficient method in modeling the contact mechanics of articular cartilage. But due to the high deformability of the menisci, modeling the menisci in the multi-body environment is a challenging process. Therefore modeling the

menisci is avoided in many multi-body computational studies (Bei et al, 2004). However, a larger number of studies model menisci in the FE environment (Peña et. al, 2006).

This manuscript presents two separate studies designed to develop a multi-body model of the human body to simulate ambulatory activities such as gait. The goal of the computational method is to predict the loading environment of a knee with menisci in a multi-body computational framework during gait.

Chapter two presents a method to calculate the resting length or zero load length of the bundles of ligaments of the knee using an iterative process. A multi-body computational model of the right leg of the subject is developed using magnetic resonance imaging (MRI) of the lower leg in addition to the motion measurements of the lower and upper leg in the kinematic envelope of motion.

Chapter three presents development and validation of a full body computational model of gait using the data from chapter two in addition to motion data recorded from the subject during the gait trial. Ground reaction forces (GRF) recorded from force plates in the ground and the joint angles during the Inverse kinematic simulation are used as means of validation for the model. Following the validation of the model by comparing the ground reaction forces predicted by the model and measured during the experiment, two different objectives were achieved.

1. Patellofemoral pressure distribution was studied in response to manipulation of patellofemoral tendon, both in terms of insertion and laxity of the tendon to analyze two pathological situations.

2. The motion of menisci with respect to the tibia was examined during gait in response to different horn attachments' stiffness.

Chapter Four presents a conclusion and summarizes the points covered in the manuscript.

Chapter 2

Resting Length of Knee Ligaments in a Subject Specific Model

Introduction

The knee joint is one of the most important joints in the body and it is vulnerable to both acute and chronic injuries. ACL rupture, the most common knee injury [Woo et al. 2002], accounts for approximately $3 billion dollars of healthcare cost each year [Brophy et al. 2009]. ACL injury leads to kinematic changes in the knee, leading to abnormal loading distribution of contact pressure on the articular cartilage [Imhauser et al. 2013]. Due to this change in the contact area, some of the areas that have not been under compression loads take loading and also the loading is reduced in some areas. Andraicchi et al. (2004) suggested that changes in mechanical loading of the joint results in the onset and progression of OA. Chronic debilitating conditions such as OA and patellofemoral pain syndrome are also very common. OA affects over 20% of adults over the age of 25 in the hip or knee [Helmick et al. 2008].

Understanding this mechanical environment requires a deep knowledge of the interaction of soft tissues, mainly articular cartilage, menisci and the ligaments. However in-vivo measurement of forces acting on the ligaments, articular cartilage and menisci is not feasible. Computational models on the other hand provide researchers with tools that enable them to study almost every aspect of joint biomechanics.

Ligaments are often modeled as bundles of elastic nonlinear springs, with a piece-wise function, modeling the two elastic loading regions; nonlinear toe region and linear region [Blankevoort et al. 1991 and Guess et al. 2014]. The toe region ends when all of

the fibers have become taut [Weiss et al. 2005] and the ligaments can be modeled as a constant stiffness linear spring.

The length at which the ligament starts carrying load (the beginning of the toe region) is called the ligament resting length or the zero-load length. Previous sensitivity studies conducted in our lab suggest that the predicted force in the ligament is highly sensitive to the zero-load length. It has been established by Berozzi et al. (2008) that the changes in the ligament reference length (Length of the ligament at reference position, usually full extension) affect the laxity of the knee model significantly. Moreover, Baldwin et al. (2009) identified the reference strain (strain of the ligament at reference position) as a critical property affecting the knee model. Reference length and the reference strain are both related to zero-load length. Therefore, calculating an accurate value for the ligament resting length in each bundle is crucial in developing a computational musculoskeletal model.

This chapter presents a method to measure this length for each of the ligament bundles using MRI and motion data recorded during the knee laxity test (the procedure that attempts to move the joint in the range of motion without applying force to the joint).

The geometries of the right leg were created from MRI in 3D Slicer (www.slicer.org) and post processed in Geomagic Studio (Geomagic, Inc. Research Triangle Park, NC). A multi-body model of the lower leg was created in a multi-body framework in MD Adams (MSC Software Corporation, Santa Ana, CA). An iterative bi-section root finding method was used to find the value of the zero-load length. A simulation was performed using the motion measurements of the laxity test. The forces predicted at each step were examined and if the forces during the simulation were over the threshold (50 N), the zero-load

length of that bundle was increased to the mid-point of the previous zero-load length and the maximum distance of the insertion and origin of that bundle. The simulation was performed 10 times until all of the predicted forces were below 50 N.

The final zero-load length values, as well as a normalized zero-load length for each ligament bundles, are presented. The ligament length for each bundle is shown for flexion angles of up to 120°.

Methods

Experimental Procedure

The Experimental Procedure was conducted by researchers in the Musculoskeletal Biomechanics Research Laboratory (MBRL) of the University of Missouri – Kansas City (UMKC). This section is presented here for the sake of better understanding the material.

A young female with no prior lower extremity injuries have been selected for the study (age: 20 years, height: 159.5 cm, mass: 59 kg). The subject signed a written consent approved by the Internal Review Board (IRB) of UMKC to participate in the study.

Two Bone Localizers, one for Tibia and one for Femur were fitted on to the subject prior to MRI. The purpose of the localizers is to register segments of lower body to the motion capture coordinate system for modeling purposes. Radius of curvature was different between the localizers in order to fit the upper leg and lower leg properly. Mustard is visible in the MRI and it was used in the two orthogonal hollow tubes inside the localizers. Those cylinders were later used in developing the computational model to register the bone geometries to motion capture data (Figure 2.1).

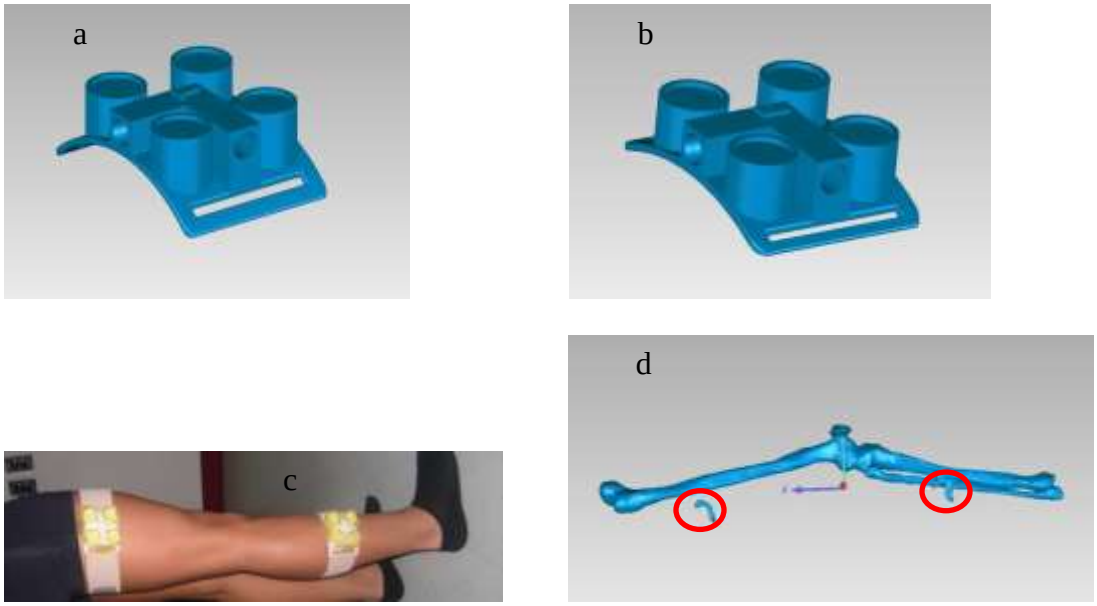

Figure 2.1. Custom Designed Localizers. Femur localizer (a) and tibia localizer (b) are attached to the right leg of the subject (c). The cylinders that are filled with mustard show up in MRI (Red circles in d) and are used to align the localizer geometries to bone geometries.

The localizers have 4 small spots that house reflective markers. After the MRI four markers are attached in order to capture the motion of the lower and upper segments of the leg. A second localizer was attached on the shin bone in order to provide better information on the location of the lower body. Since there is almost no soft tissue on the shin bone, the markers attached to the second localizer provide more accurate information with less skin artifact (Figure 2.2).

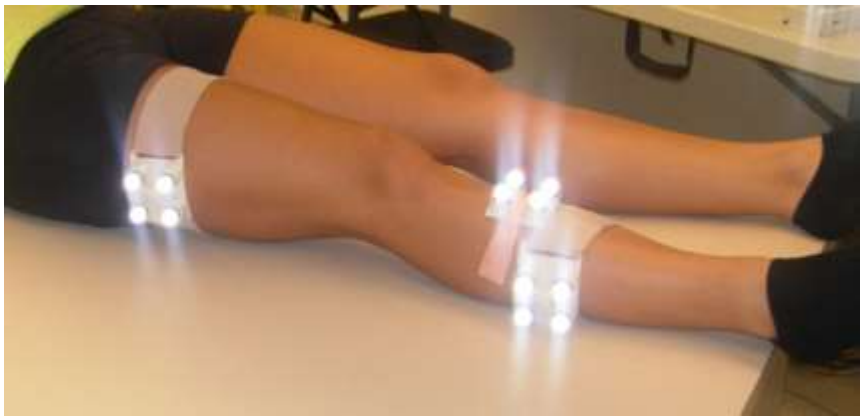

Figure 2.2. A second localizer is attached to the tibia on the shin bone. The shin localizer has less skin artifact

In the next step a surgeon manipulated the knee in the whole range of motion in order to examine the kinematic envelope of motion (KEM). The subject was instructed to lay on their back and relax their leg muscles while the surgeons was moving the knee through the complete range of flexion-extension, abduction-adduction and internal-external rotations in addition to translation in anterior-posterior, medial-lateral and vertical direction. The surgeon was instructed to minimize the force on the passive elements of the knee.

Computational Model

After the imaging, 3D Slicer was used to segment the geometries from MRI. The geometries were saved as STereoLithography (STL) files. Post processing of the geometries such as smoothing, reducing noise, removing spikes, removing tunnels and holes was performed using Geomagic Studio. The final geometries are shown in Figure 2.3.

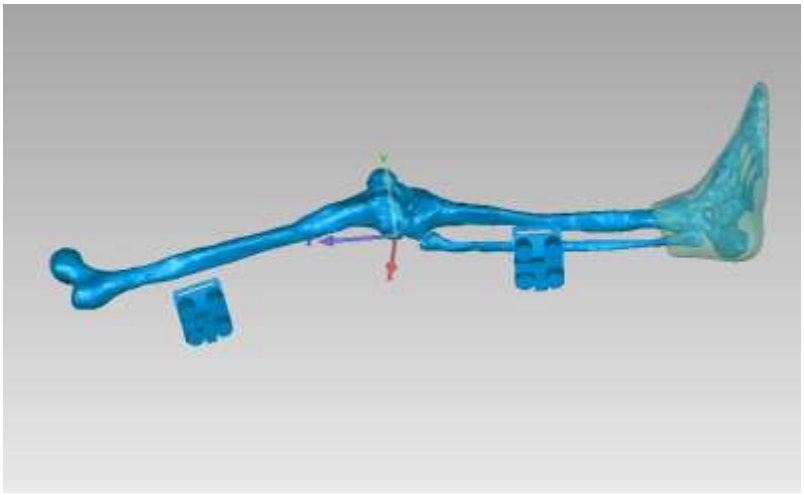

Figure 2.3. Geometries are post processed in Geomagic to remove the surface defects.

In order to model the contact mechanics of the articular cartilage, the modeling software, MD Adams calculates the penetration and the speed of penetration of the geometries (Equation 2.1). The only geometries that were used to define the contacts were femoral cartilage and tibial cartilage. Therefore, the surface of those geometries should match the MRI exactly. In the rest of the geometries, the number of surface elements was reduced as much as possible to help reduce the size of the files, making the model more efficient. In the geometries that were used to define contact (Tibial and femoral cartilage); the number of surface elements were reduced as well. However, the majority of the reduction in size is only performed on the side that is not involved in any contact interactions. For example, the number of elements in the upper side of the femoral cartilage (concave side) is significantly reduced while the articulating side is only slightly reduced (convex side). The final element count between 10,000 and 20,000 provides an appropriate file size and also simulation time. It should be noted that after the final processing of the geometries, all of them were imported into the Slicer environment and the surface of the geometries were compared against the MRI.

A multi-body computational model of the right leg was created from the geometries in the MRI position in the MD Adams environment. The femoral and tibial cartilages were attached rigidly by a fixed joint to the upper leg and lower leg respectively. The fixed joints are located at the center of mass for each cartilage part which is calculated automatically in ADAMS based on the volume and the density (1.08E-006 kg/mm^3) of the geometry. Contact force elements are created between tibial articular cartilage and femoral articular cartilage. The contact force is predicted by combining a Hertzian contact model with a damper to allow for energy dissipation [Sharf and Zhang 2006]. Contact force is defined as a function of geometry penetration depth and penetration depth velocity:

$$\text{Equation 2.1.} \qquad F_c = k\delta^n + B(\delta)(\dot{\delta})$$

Where F_c is the contact force, k is the contact stiffness, B(δ)is the damping coefficient, k is the contact stiffness, δ is the penetration of the contacting geometries and $\dot{\delta}$ is the velocity of interpenetration. Contact parameters in the tibio-femoral joint have been found by a recent optimization study to be Kc = 327, B = 5 and n = 2.07[Guess et al, 2010]. In that optimization study, contact parameters were systemically modified as design variables so that the multi-body model prediction matched the model of the same knee in the finite element environment.

The ligaments were represented as one-dimensional nonlinear springs. The model included two bundles for the ACL and posterior cruciate ligament (PCL). The Lateral Collateral Ligament (LCL) was divided into three bundles. The Medial Collateral Ligament (MCL) was modeled to define the functions of both deep and superficial bundles of the ligament. The deep bundle is divided into two bundles (anterior and posterior DMCL) and the superficial bundle is divided into three bundles (anterior,

intermediate and posterior SMCL). Ligaments were attached to bone based on the origin and insertions identified from the MRI. A complete overview of ligament attachments and mechanical properties has been presented in Appendix 1. Ligament Force elements predict the force by combining the static and dynamic response of the ligament to movement of lower leg relative to upper leg.

The static response is defined based on the force length relationship described by Blankevoort (1991) and Wismans J (1980).

$$\text{Equation 2.2} \qquad F = \begin{cases} 0 & \varepsilon < 0 \\ \frac{1}{4} k\varepsilon^2/\varepsilon_1 & 0 \le \varepsilon \le 2\varepsilon_1 \\ k(\varepsilon - \varepsilon_1) & \varepsilon > 2\varepsilon_1 \end{cases}$$

Where $\varepsilon = (\frac{l-l_0}{l_0})$ is defined as the engineering strain. K is a stiffness parameter with dimension of force. Table 3.2 presents the values used for k in different ligaments of the knee. ε_1 was assumed to be 0.03 in order to include the non-linear toe region of the force-length curve [Li G et al. 1999]. The objective of this study is to calculate an accurate value of l_0, the zero-laod length. The initial value for l_0 was set to the distance between the insertion and origin of each bundle measured from MRI.

The active component of ligament response is defined as a parallel damper. The damping coefficient is different when the ligament is lengthening and shortening. Damping coefficient for lengthening is assumed to be 0.5 Ns/mm while the value for shortening was assumed to be 0.01.

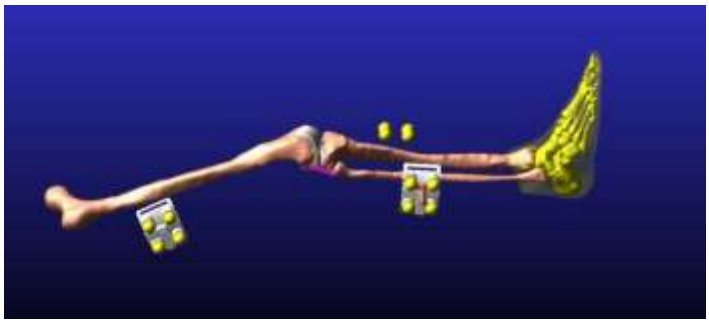

Figure 2.4. Musculoskeletal model illustrating ligaments as cylinders and motion constrains as yellow.

The motion data during the laxity test records the location of each motion marker in space. There may be a difference between the relative location of localizer and bone between MRI and the laxity test. This difference is caused by the movement of soft tissue beneath the markers also known as the skin motion artifact [Nester et al. 2007].

In order to address this problem, an equilibrium simulation was performed. Femur and tibia localizer geometries were imported into the model as individual parts. The lower leg and upper leg were attached to the localizers via a 6 degree of freedom spring parallel with a damper. Such element is defined as a Bushing element in Adams. Each of the motion markers were also attached via a bushing to four motion markers. The stiffness and damping of mentioned bushing are presented in the Table 2.1. The bushings between body segments and localizers are defined at a single location (2 parts 1 Location). However, the bushing between the motion markers and localizers are defined between two different locations (2 Parts 2 Points). This equilibrium (10 seconds of simulation) allows the localizers to move slightly in the space to match the "best fit position" before starting the simulation of laxity test.

After adjusting the location of the localizers relative to the bone, the localizers were rigidly attached to the bone by deleting the bushings between the localizer and the leg segments and replacing them with fixed joints. The stiffness of the bushings between

motion constraints and the localizers were reduced too. The stiffness and damping values for the bushings are presented in the Table 2.1.

	Bushing between body segment and localizer	Bushing between motion marker and localizer	Bushing between motion marker and localizer After Equilibrium
Translational Stiffness	80	100	10
Translational Damping	10	10	1
Rotational Stiffness	10	100	0
Rotational Damping	1	10	0

Table 2.1. Stiffness and Damping values of Bushing elements.

Simulation

An iterative procedure was performed to determine the zero-load length for each ligament bundle. The goal was to reduce the load taken by each ligament bundle during the simulation. Despite the careful manipulation of the surgeon while performing the laxity test, ligaments carry a minimal load through the KEM. Therefore, a threshold of 50N was set and the objective of the study was to reduce the maximum load on each ligament bundle during simulation below the threshold. 50N corresponds to 3-5.5% ligament strain which is approximately the ligament strain at the transition between nonlinear to linear portions of the force length relationship.

At each iteration step, a simulation of knee laxity test was performed (approximately 2 minutes simulation) with a step size of 0.01 s. Each simulation takes about 40 seconds on a machine with Intel Core i7-4770 @ 3.40 GHz with 16.0 GB of RAM. The forces carried by each ligament bundle and also the distance between origin and insertion of each ligament were recorded during the simulation.

If the predicted force carried by a ligament bundle stays below 50N, the zero load length stays the same in the next iteration. However, if the force reaches values above

50N, zero-load length for that specific bundle is increased to the midpoint between the previous value and the maximum length recorded.

The iterations stop at a point where all of the ligaments predicted tension values are less than 50N. The zero-load lengths in the final step are recorded as the subject specific zero-load lengths for each bundle. It should be noted that contact between the tibial cartilage and femoral cartilage was maintained during the simulation.

Results

It took ten iterations for the model to reach the goal where the forces carried out by all the ligament bundles were below 50 N during the simulation of KEM. The values in the first iteration (distance between insertion and origin of each bundle in MRI) as well as final values are presented in the table below.

	MRI origin and Insertion Distance	Final Zero-Load Length Values
AM-ACL	33.4	35.23
PL-ACL	25.7	26.43
AL-PCL	35.8	42.31
PM-PCL	35.4	46.31
A-LCL	46	52.03
I-LCL	46.7	53.63
P-LCL	43.9	51.86
A-SMCL	90.1	94.38
C-SMCL	91.9	93.58
P-SCML	94.3	96.98
A-DMCL	34.7	40.91
P-DMCL	33.8	36.76

Table 2.2. Distance between the insertion and origin and the zero load length of each ligament bundle

The distance between the medial and lateral condyles of the femur (74.2mm) was used as a measure of the knee joint size to normalize the data for comparison purposes. Ligament bundles lengths were graphed against the flexion angle in Figure 2.5.

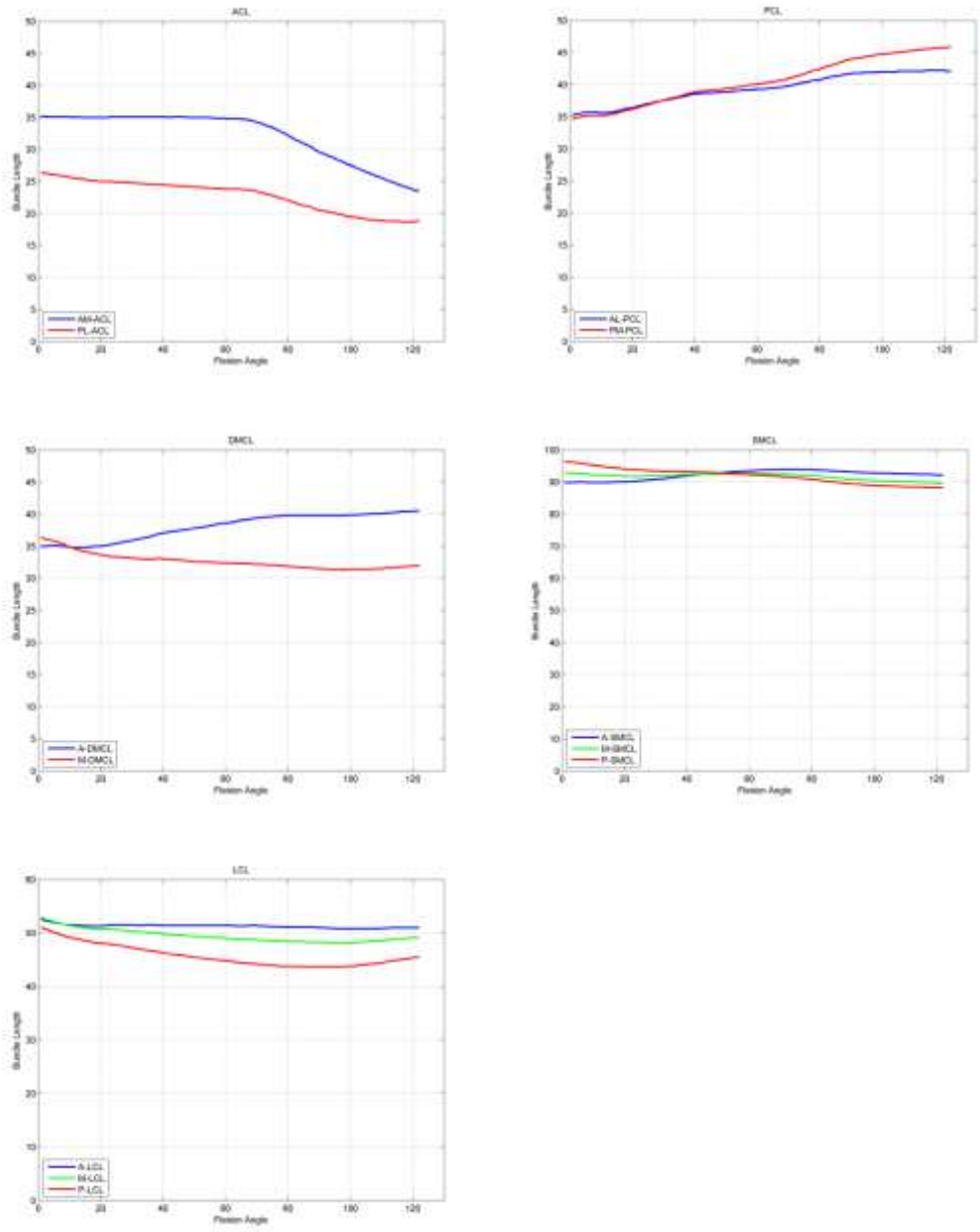

Figure 2.5. Ligament bundle lengths versus function of flexion angle.

Discussion

The length at which the ligaments start carrying loads, called ligament resting length or zero-load length, is an important parameter in computational biomechanics. In computational modeling, zero-load lengths usually come from cadaveric studies and are not subject specific. This chapter presents a method that can calculate subject specific zero-load lengths using MRI and knee laxity measurements conducted in a gait lab.

Numerous computational studies use the same force-length relationship (Equation 2.2) [Baldwin et al., 2009; Guess et al., 2010; Li et al., 1999; and Yang et al., 2010]. Few researcher [Yang et al., 2010] have used the previously published reference strain (ε_r) values published by Blankevoort et al. (1991) to predict the force in the ligament. Reference strain is the strain in the ligament at a reference position (usually full extension of the knee). These generalized values will not take the subject variability into account and therefore developing a subject specific model using this method is not desired. Other researchers have used optimization methods that compare the results predicted by the model to experimental results. Despite the effectiveness of this method for in-vitro modeling [Li et al., 2002], using this method for in-vivo subject specific modeling is not feasible.

The same method discussed in this chapter was performed on two other female subjects by other researchers (Subject 2: Age: 22, Height: 172 cm, Weight: 73 kg and Subject 3: Age: 29, Height: 170 cm, Weight: 70kg). The medial-lateral distance of knee condyles was measured to be 81.0 mm and 73.49 mm respectively. The reported zero-load length values are presented in Table 2.3.

Ligament Bundle	Subject 1	Subject 2	Subject 3	Mean (SD)
AM-ACL	35.23	46.16	37.25	39.55 (5.82)
PL-ACL	26.43	40.26	30.51	32.40 (7.11)
AL-PCL	42.31	49.14	52.20	47.88 (5.06)
MP-PCL	46.31	57.56	44.64	49.50 (7.03)
A-LCL	52.03	61.52	66.61	60.05 (7.40)
I-LCL	53.63	57.66	64.51	58.60 (5.50)
P-LCL	51.86	55.35	60.67	55.96 (4.44)
A-SMCL	94.38	101.02	95.69	97.03 (3.52)
I-SMCL	93.58	102.21	94.54	96.78 (4.73)
P-SMCL	96.98	106.60	96.36	99.98 (5.74)
A-DMCL	40.91	37.68	46.78	41.79 (4.61)
P-DMCL	36.76	38.25	38.89	37.97 (1.09)

Table 2.3. Zero load length for each ligament bundle across 3 subjects.

These values differ among subjects. However, normalizing these values to the medial-lateral distance of the knee as presented in Figure 2.6 illustrates consistency between the results derived for each ligament bundle. The figure suggests that the normalized zero-load lengths for each bundle can be used as a starting point in computational models in the development phase.

Figure 2.6. Normalized ligament zero-load length is consistent between subjects.

Guess et al. (2013) performed a similar method on a cadaver specimen by measuring the maximum ligament length during a knee laxity test and reported zero-load length of the ligament bundles as a percentage of that value. The zero-load length for cruciate ligament bundles was set at 85 percent of the maximum measured length of each bundle

while it was set at 80 percent of the maximum measured length for the collateral bundles. They reported zero-load length values of 34.9 mm and 25.1 mm for AM-ACL and PL-ACL respectively. The average ligament zero-load length between the three subjects calculated by the current method was 39.55 and 32.40 for those bundles. Zero-Load length values of 29.8 mm and 35.9 mm were reported for AL-PCL and PM-PCL bundles of the cadaver specimen while the average values from the current method between the three subjects was 47.88 mm and 49.50 mm for AL-PCL and PM-PCL bundles respectively. The ligament resting length of LCL bundles were 50.4 mm, 48.8 mm and 49.6 mm for A-LCL, I-LCL and P-LCL respectively. The average of the reported values from current study was 60.05 mm, 58.60 mm and 55.96 mm for the LCL bundles. MCL was modeled as a three ligament bundle in the cadaveric study. The values reported in the cadaveric study were 82.4, 81.6 mm and 80 mm for the anterior, middle and posterior bundles of the MCL respectively, which corresponds to the superficial MCL bundles in the current methods. The average superficial ligament bundled length derived from the current study was 97.03mm, 96.78 and 99.98 mm for A-SMCL, I-SMCL and P-SMCL respectively.

Agreement between results of a cadaveric study and the current in-vivo study as well as consistency between the normalized zero-load length values (Figure 2.6) demonstrates that the method presented in this chapter can be successfully implemented for subject specific modeling purposes.

Several cadaver studies have examined the length of the ligaments and have reported length variations relative to different flexion angles. These reported values may not be directly comparable to the results presented in this chapter. However, the value of the

zero-load length can be compared to the maximum reported length in those studies to further validate the results of the current study.

In a systematic review of ACL anatomy, Duthon et al. (2006) reported a range of 22 to 41 mm for ACL. Zero-load length of the ACL bundles predicted by the present computational model (39.55 mm and 32.40 mm), fall between these values.

Bowman and Sekiya (2009) examined the functional anatomy of PCL and reported values of 35.5 mm and 38.7 mm for AL-PCL and PM-PCL bundle. Defrate et al. (2004) reproduced the in-vivo motion of the knee to study the function of PCL in-vivo. They observed a maximum length of PCL at 90 degree flexion (35.3±2.4 mm) while the minimum length occurred at 0 degree flexion (28.7±1.5mm). During the simulation in our study, both of PCL bundles have a minimum length at 0 degrees. AL-PCL reaches the maxim length at about 90^0 of flexion while PM-PCL increases length to reach the maximum length at about 120^0 of flexion.

Laprade et al. (2007) measured the superficial bundles of the MCL and reported a range of 100-120 mm over eight cadaver specimen. Park et al. (2005) examined the range of motion of the knee using MRI and fluoroscopy data over five healthy subjects during a quasi-static lung from 0^0 up to 90^0 of flexion. The superficial layer of MCL was divided into three bundles. The A-SMCL was 66.8±4.9 mm at full extension and increased to 68.9±3.3 mm at 90^0 of flexion; length of I-SMCL decreased from 76.0±4.1 to 71.1±3.4 mm from full extension to 90^0 of flexion; and length of P-SMCL decreased from 87.9±4.9 to 74.4±4.4 mm from full extension to 90^0 of flexion. Our computational model predicted the same trend for A-SMCL and P-SMCL; A-SMCL increasing from 88.7±3.5 mm to 95.2±1.3 mm and P-SMCL decreasing from 96.6±3.0 mm to 93.7±2.2 mm from

full extension to 90^0 of flexion. However, M-SMCL increased from 93.2±2.6mm to 94.2±1.0 mm with no significant difference.

In the Park et al. (2005) study, deep layer of MCL was divided into three bundles too (In contrast to our model with two deep MCL bundles). A-DMCL was 24.9±4.8 mm long at full extension and increased in length to reach a maximum of 29.2±4.4 mm at 90^0. A-DMCL decreased from 30.1±3.7 mm at full extension to 25.0±3.8 mm at 60^0 of flexion and then increased to 26.3±3.6 mm at 90^0 of flexion. The P-DMCL was 34.2±3.9 mm at full extension and the length reduced to 26.5±mm at 30^0 of flexion and reaching a minimum of 22.8±3.9 mm at 90^0. Our model divided the DMCL into two bundles, predicting a similar pattern; the A-DMCL increased from 34.2±0.6 mm to 40.7±2.4 mm and P-DMCL decreased from 35.4±1.8 mm to 32.2±1.3 mm from full extension to 90^0 of flexion.

Park et al. (2005) also studied the LCL and separated in three bundles. A-LCL was 54.1±6.6 mm at full extension and increased to 57.9±6.9 mm at 90^0 of flexion; I-LCL was 53.6±7.1 mm at full extension and decreased to 52.7±6.7 mm at 90^0 of flexion; and P-LCL was 53.1±6.6 mm at full extension and decreased to 47.7±6.1 mm at 90^0 of flexion. A similar trend was observed in our computational model, measuring the LCL bundles from full extension to 90^0 of flexion. A-LCL increased in length from 57.1±3.0 mm to 54.1±3.3 mm; Length of I-LCL was reduced from 57.3±2.8 mm to 54.1±3.3 mm; and length of P-LCL reduced from 54.6±2.0 mm to 48.5±3.0 mm.

Limitations of this study include the limited population of the subjects (The method has only been applied to three young female subjects). Moreover, all of the ligament bundles were modeled as two point forces. Therefore, wrapping was not modeled in the

current study and due to the fact that the superficial MCL wraps around the medial condyle of the tibia, the line of action of superficial MCL was not properly modeled. Modeling the wrapping of SMCL should be examined in future works. In addition, the bisection method was used in the optimization process. Other root-finding methods may reduce the number of iterations. Another piece of information missing in the modeling process was the force applied to the leg by the examiner. However, directly measuring the force may be difficult.

Chapter 3

Development of a Subject Specific Full Body Musculoskeletal Model

Introduction

Knee injuries whether stemming from an impact injury such as ACL ruptures or chronic disorders stemming from wear and tear of cartilage and menisci such as OA have a high occurrence in the population. Knee injuries are even more common among people with increased physical activity. Understanding the interactions of soft tissues in the knee during everyday activities is important in improving the design and outcomes of non-invasive therapies as well as more invasive techniques such as joint arthroplasty and allograft replacement. Concurrent musculoskeletal models in multi-body framework predict the muscle forces as well as joint loading concurrently, thus, providing a deep understanding of the soft tissue biomechanics.

Patellofemoral Biomechanics

Devereaux and Lachman (1983) reported that incidents of patellofemoral pain are among the highest of knee pain reports. Daily ambulatory activities are severely limited due to patellofemoral joint diseases [Wunschel et al. 2011]. Fulkerson & Shea (1990) suggested that patellofemoral pain may be a result of increased patellofemoral cartilage contact pressure. However, calculating patellofemoral contact pressures has proven to be challenging in-vivo.

Different experimental and computational studies have been performed to examine the complex biomechanics of the patellofemoral joint. For example, Lee et al. (2002)

examined five cadaver specimens to study the effects of vastus medialis (VM) muscle strength on patellofemoral joint kinematics, contact pressure and areas. Goudakos et al. (2010) developed a method to directly measure the patellofemoral contact stress and contact area in cadavers by simulating the motion of subjects by using forces from computational models. Computational models have been used to model the PF joint mechanics too. However, they are usually limited to specific loading condition scenarios and not ambulatory activities. Several multi-body and FE models of the knee have been developed recently to enhance our knowledge of soft tissue biomechanics. For example, Bei and Fregley (2004) introduced a concurrent multi-body musculoskeletal model that predicted muscle forces and joint contact pressures. They incorporated a deformable contact knee model (without menisci) into a rigid-body multi-body framework. These studies examine the mechanics of the patellofemoral joint under specific loading conditions and are unable to provide information on the subject specific contact pressure distribution during daily activities such as gait. Some studies have estimated the total contact force between the patellar and femoral cartilage and used MRI to calculate the joint contact area in-vivo, thus calculating an average contact pressure in the patellofemoral joint [Ward and Powers 2004]. Although this method provides a good understanding of overall joint mechanics, it falls short of providing details about peak pressure values or pressure distribution in the joint. FE models have been used to predict the contact pressure in the knee (Besier et al. 2005). But FE models are computationally intensive and it is difficult to implement an FE model into a full-body musculoskeletal model to simulate ambulatory activities. Specific static or quasi-static loading condition such as anterior loading or a combined valgus and internal moment is usually used as

input into these models and the active muscle forces are not included in the modeling process [Mootanah et al. 2015]. In contrast, multi-body musculoskeletal models of the human body are computationally efficient and several muscle force prediction schemes have been suggested in the literature. However, the degrees of freedom in joints are usually reduced, inhibiting the researcher to study the complex nature of soft tissue biomechanics under loading conditions of ambulatory activities.

Menisci Biomechanics

The menisci reduce the pressure on tibial cartilage by increasing the contact area in the knee, thus, distributing the contact pressure over a larger area of the cartilage. Menisci also provide stability and shock absorption to the knee [Brindle et al. 2001].

In-vitro studies (cadaveric studies) examine the mechanics of the menisci and provide valuable insight into the interaction of menisci with other soft tissues of the knee. However, in cadaveric studies, the loading applied to the knee is static or quasi-static and not the dynamic physiological loads that are applied to the knee during daily activities [Seitz et al. 2012 and Wunschel et al. 2012]. Moreover, the sensors that measure the contact pressure may change the biomechanics of the joint.

In-vivo studies (radiographic studies) examine the function and also location of the menisci on the tibia. For example, Stehling et al. (2012) studied the medial meniscal extrusion (extension of meniscus beyond the tibial margin) by comparing the MRI of the loaded knee against the unloaded knee. They associated the medial meniscal extrusion with knee OA. Several MRI studies were performed on unloaded knees [Wenger et al. 2013] and studies that examined the anatomy of the loaded knee only looked at the knee under specific loading conditions.

In-silico studies that predict the deformability of menisci and cartilage in the knee are often developed in FE framework. However, FE models are computationally intensive and they usually do not predict muscle forces. Therefore, only simplified loading conditions are applied to them and biomechanics of the soft tissue is not examined under physiological loads. Contrary to FE models, computational models that are developed in the multi-body framework are able to predict the muscle forces and tibio-femoral contact mechanics concurrently. Because of the high deformability of the menisci, modeling the menisci in the multi-body framework is a challenging process and the menisci are not modeled [Arnold et al. 2010].

In this chapter, a multi-body computational full body model of a human subject was developed that includes the menisci to study the contact pressure and contact area in the patellofemoral joint as well as biomechanics of the menisci. The goal of the study was to develop a full body musculoskeletal model in the multi-body framework to concurrently predict the muscle forces of the lower body as well as knee ligaments and contact forces during gait. A 3-D subject specific model of the knee that included femoral, tibial and patellar articular cartilage as well as lateral and medial meniscus geometries in addition to knee ligaments was implemented into a multi-body computational model. The musculoskeletal model examines the biomechanics of the knee. The model can be manipulated to simulate different "what if" scenarios, enabling us to examine the biomechanics of the different pathological conditions. The first goal of the study was to examine the patellofemoral contact pressure distribution of the knee. The second goal of the study is explore the biomechanics of menisci in response to laxity of the horn attachments.

After the experimental testing (conducted by other researchers), geometries of the bones in the lower body, as well as knee soft tissues were created in 3d Slicer. Geometries were post processed in Geomagic and imported into a generic computational model in MSc ADAMS. Two different simulations were performed. First, the Inverse Kinematic simulation, which the motion constraints moved the body segments while the joint angles and muscle lengths were being recorded. A Forward Dynamics simulation was then performed in which the recorded values in the previous phase were used in a feedback control scheme to calculate the muscle forces and joint angles. The simulations were performed in Simulink.

A Normal model was created based on the MRI. The ground reaction force predicted by the model is compared against the experimental forces measured in the gait lab. Moreover, the angles of the joints are compared to the Inverse Kinematic simulation.

Three pathological patellofemoral conditions were modeled; Patella Alta (high patella riding), Patella Baja (low lying patella) and a knee with tibial tuberosity-trochlear groove (TT-TG) distance of more than 20 mm. The contact mechanics were compared against the Normal model.

Four models were created to study the mechanics of the menisci by changing the length of the menisci horn attachments. The difference between the load transfer as well as menisci extrusion and excursion is examined in those models.

Method

Gait Lab Testing

The experimental procedure was conducted by researchers in the MBRL at UMKC. This section is presented here for the sake of better understanding the material.

The gait lab testing and Imaging was performed on one young healthy female (Age: 20, Weight 59 kg, Height 159.5) with no prior lower extremity injuries. A written informed consent approved by the IRB of UMKC was provided to the subject before the experiment.

After the MRI and laxity test, covered in chapter 2 of this manuscript, reflective markers were attached to the subject based on the plug-in-gait marker placement protocol. In addition to the plug-in-gait markers, a set of additional markers were attached to the subject in order to facilitate the modeling process. The extra markers include four on the right femur localizer, four on the right tibia localizer, one on the left upper leg and one on the left lower leg, one on medial side of each ankle (attached on the medial malleolus), and one on each of metatarsals (attached on the fifth metatarsal). Plug-in marker placement requires either attaching two markers to Left and Right Posterior Superior Iliac Spine (LPSIS and RPSIS) or sacrum (SACR) marker. However, all of those three markers were attached in the experiment.

Moreover, eight surface EMG electrodes were placed on the muscles of the right leg. These muscles include Gluteus Maximus (GMax), Biceps Femoris (BF), Vastus Medialis (VM), Vastus Lateralis (VL), Gastrocnemius Lateralis (GL), Gastrocnemius Medialis (GM), Tensor Fascia Latae (TFL), and Tibialis Anterior (TA). In addition, the gait lab

was equipped with 4 OR-6 force plates (AMTI, Watertown, MA) to measure the resultant reaction force and torque as well as center of pressure.

Figure 3.1. In addition to plug in gait marker placement protocol, additional markers are attached to the subject.

The subject went through several ambulatory activities including squat, side cutting maneuver, jogging, self-paced gait and a trial of Static Pose with arms wide open. Motion data from the reflective markers, ground reaction forces, and EMG signals were recorded. Following the gait measurements, a System 4 Pro dynamometer (Biodex, Shirley, NY) was used to obtain the maximum voluntary contraction (MVC) of each of the muscle groups mentioned above. MVC signals may be used to calculate the level of muscle activation during ambulatory activities.

Figure 3.2. Subject poses in a static trial that will be later used to adjust the location of marker placements to the body segments.

A trial of self-paced bare foot walking trials were the subject hit different force plates during each step was selected for modeling purposes.

Figure 3.3. The subject performs several ambulatory activities in the gait lab.

Computational Model

The subject specific computational model presented here was created by modifying a generic computational model and adding subject specific geometries to it. In the following, developing the generic model is explained followed by the subject specific model and the simulation process.

Generic Model

A generic multi-body musculoskeletal model of the subject was built based on the height, weight and sex of the subject.

In the first step, a previously created macro was used to bring in the generic geometries of each body segment (scaled by the height of the subject) (Figure 3.4 a). In order to find the mass and inertia properties for each of the body segments and to also find the location of joint centers, the macro created 32 anthropometric measures based on the regression equations from Generator of Body Data (GEBOD) program. Appendix 2 of this manuscript presents information on anthropometric equations and GEBOD. The current computational model consisted of two extra body segments compared to the GEBOD program, the right scapula and the left scapula. Therefore, modifications were implanted in the macro to address the difference. Each body segment was first fitted with an ellipsoid created based on the 32 anthropometric measurements (Figure 3.4 b). The total volume of all ellipsoids was measured and a mean density was calculated by dividing the total volume of ellipsoids by the weight of the subject. Mass and inertia properties were generated automatically by assigning the calculated mean density to each body segment. Center marker locations and the dimensions of all ellipsoids are also presented in Appendix 2.

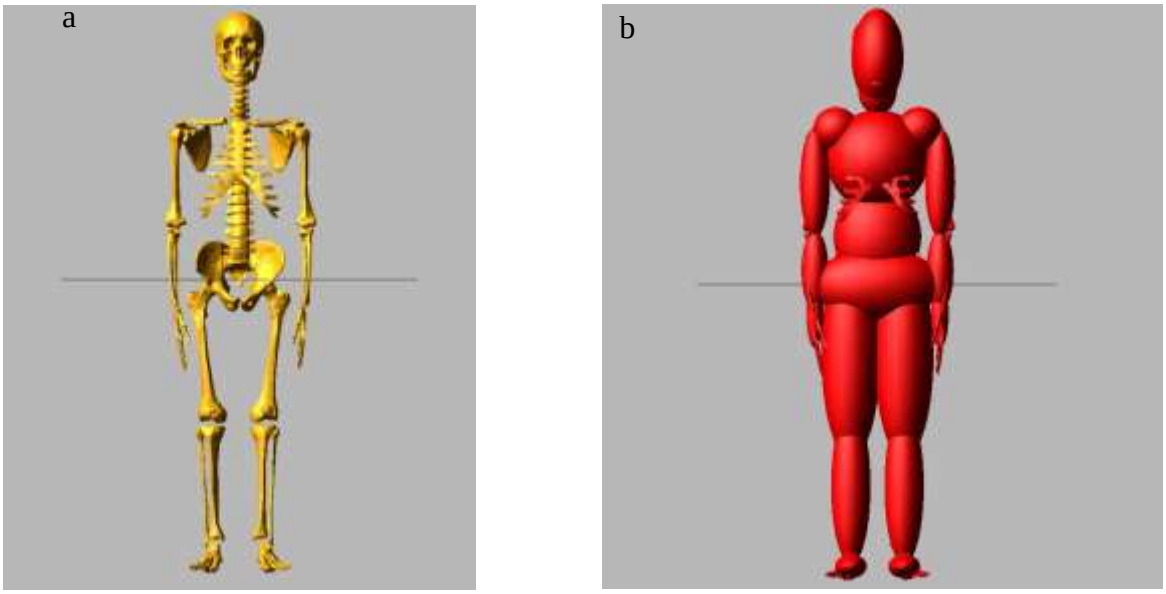

Figure 3.4. The generic model is built by scaling generic geometries to height of the subject (a). Mass of each body segment is assigned based on the volume of the generic ellipsoids (b).

The macro was then used to create the elements required to model the joints of the body. Each joint was assumed to be a spherical joint and was created using three perpendicular revolute joints located at a single point. Defining a joint in this manner will enable us to measure the joint rotation around each axis and also apply torque to each axis independently. Since it is impossible to define more than one joint on the same location between two bodies in ADAMS, two dummy parts with negligible mass and inertia (m=1.0001E-4 (kg) and I=0.9999(kg.mm^2)) were defined at the center of each joint to accommodate the three revolute joint configurations(four bodies are required for three joints). Each of the revolute joints was accompanied by a measurement element to record the rotation and also a torsional spring to model the passive soft tissues of joints. The torsional spring stiffness was set at 100 (N mm/deg) and torsional spring damping was set at 20 (N mm sec/deg). Moreover, there was a torque actuator accompanying each revolute joint that was later used in the forward dynamics model.

The torque generating actuator was active only in the forward dynamics portion of simulation and was defined as a feedback proportional-integral-derivative controller (PID controller). The PID controller used the angle of the joint as the process variable and compared it to values recorded in the Inverse Kinematic portion of the simulation. A PID controller reproduces the desired motion by minimizing the error signal Equation 3.1.

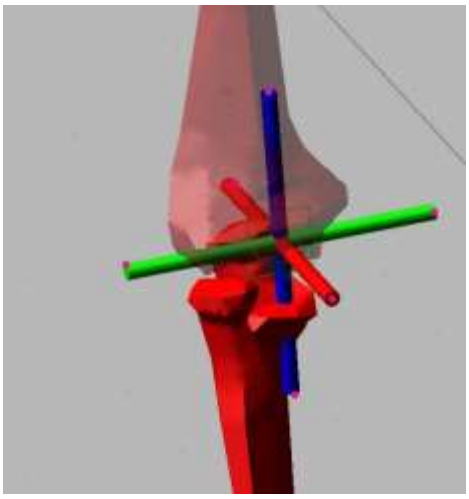

Figure 3.5. Each joint is modeled as 3 perpendicular revolute joints

$$T_i = [P.P_{error} + I.I_{error} + D.D_{error}]$$

$$P_{error} = a_{ir} - a_{ic}$$

Equation 3.1

Where $T_i$is the resulting torque for the joint i, a_{ir} is the recorded joint angle during the Inverse Kinematics, and a_{ic} is the current joint angle. The error signal; P_{error} was defined as the difference between these values. I_{error} and D_{error} were defined as the integral and first derivative of the error signal. Joint torque controller parameters for all joints were set at 30,000 1000, 0.01 and 100 for Proportion (P), Integral (I), Derivative (D) and Filter coefficient respectively. The filter coefficient determines the filter's pole location and the default value in Simulink is 100.

In order to run the Inverse Kinematics phase of the simulation, motion constraints were created and motion capture data from the gait measurements were used as inputs to move those parts in the space, thus they can only move along a prescribed trajectory.

Each of the motion parts were attached to specific body segments via bushings discussed in chapter two. The bushing between the motion constraint and the body segment models the skin artifact that is present during the gait measurements. The translational stiffness of each bushing along the principal directions was set at 10 (N/mm) and translational damping along the principal directions at 1 (N sec/mm). Since, the experimental motion is a point motion, there is rotational damping and stiffness between the motion constraints and body segments. The location of motion parts were initially picked based on a generic marker placement scaled by the height of the subject. However, location of motion parts relative to the body segments were changed to match the subject specific geometries as discussed later in this chapter.

In order to keep the balance of the subject during the Forward Dynamics simulation, a dummy rigid body was created with negligible mass and inertia (m=1.0001E-4 (kg) and I=0.9999(kg.mm^2)) on the center of mass of the pelvis (Figure 3.6).

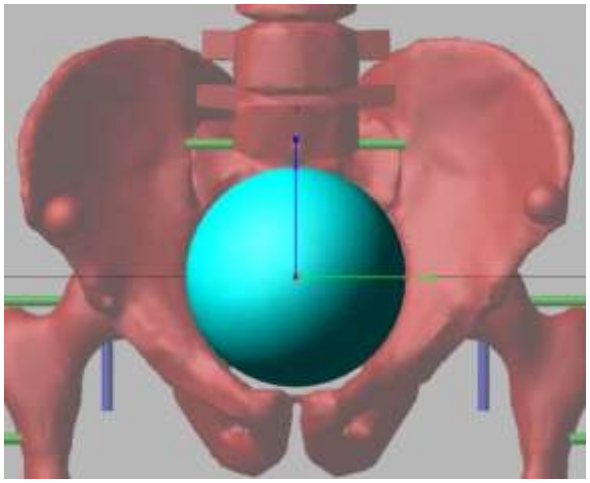

Figure 3.6. A dummy part is built in the center of mass of pelvis in order to keep the balance.

The dummy part was connected to the pelvis of the model via a six axis spring-damper (bushing). During the Inverse Kinematic simulation, the motion of the dummy part, both the location and orientation of its center of mass was recorded. During the

Forward Dynamics simulation, a general motion element drives the dummy part in the same path. However, the motion is disabled in the vertical direction to minimize the influence of the dummy on the ground reaction force and the knee contact forces. The average force of the bushing acting on the pelvis was 44 N during the walk cycle.

Transitional Stiffness	100 N/mm
Transitional Damping	0.5 N s/mm
Torsional Stiffness	1000 N mm/deg
Torsional Damping	50 N mm s/deg

Table 3.1. Stiffness and Damping of the Stabilizer bushing

Subject Specific Model

The generic model was built at full extension, 0^0 of internal-external rotation and 0^0 of valgus-varus and the subject specific geometries of the leg should be brought in the model with the same condition. However, the imaging was conducted at a different angle. Therefore, a frame of the simulation from the laxity test (Chapter 2) simulation that the flexion was 0^0, was used to build the subject specific model.

The location of the menisci relative to the tibia is changing constantly and it depends both on the knee angle and the load taken by the knee. However, in order to build the model from the MRI position, it was assumed that menisci were attached to lower leg segment and do not move from the MRI location to the build location (0^0 flexion).

The patella slides through the patellar grove of the femur and the relative location of the patella relative to the femur is a function of knee flexion angle and the quad muscle group forces. However, in order to build the model from the MRI position, it was assumed that patella was attached to upper leg segment and it does not move from the MRI location to the build location (0^0 flexion).

These assumptions may introduce some error in the model and the menisci and patella might not be in the anatomical location in the build model, but since there is some

time in beginning of the simulation before the Forward Dynamics simulation (the simulation that we export the model results from), both patella and menisci have enough time to reach equilibrium.

In order to match the subject specific geometries to the generic model, the center of the hip of the subject specific geometries was matched with that of the generic model.

However, there is a small discrepancy between the length of the leg of the subject and the generic model (The subject specific leg is 16 mm longer than the generic model's leg). Therefore, the legs were moved 16 mm higher. Also based on the MRI, the distance between the femoral head centers were 162 mm apart while in the generic model, this distance was 148 mm. Therefore, both legs were moved 7 mm laterally.

The subject specific knee joint center was assumed to be the midpoint distance from the condyles of the femur and the ankle joint center was assumed to be the midpoint of the malleoli of the lower leg. These new joint center locations were used to run the mass macro again in order to change the mass and inertia properties of the lower body to better match those of the subject. It should be noted that changes in the location of the center of mass and also mass and inertia values were negligible and this step can probably be eliminated.

In order to illustrate the motion constraints that act based on the motion measurements, two spheres were created for each motion marker; a yellow sphere that moves with the motion measurements and a red sphere that is rigidly attached to the corresponding body segment (Figure 3.7).

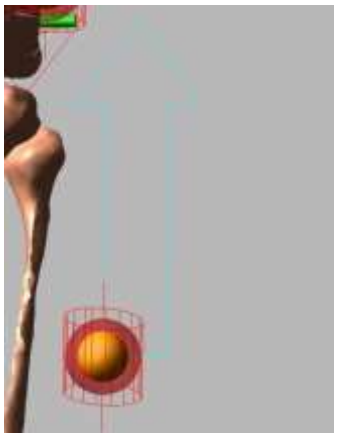

Figure 3.7. Motion constraints (yellow spheres) are attached to the body via a bushing. The red spheres illustrate the location of the marker on the body.

After importing the subject specific geometries and replacing the generic lower body geometries, the location of motion markers relative to body segments must be modified to match the marker placement in the gait lab. First, the location of lower body motion markers that were attached to bony landmarks such as the femoral condyle and ankle malleolus were modified to match the subject specific geometries. Then the motion data collected from the static trial in the gait lab was used and other lower body markers, attached to the soft tissue, such as thigh markers, were adjusted based on the gait lab static trial to match the relative location with respect to markers previously modified.

In order to adjust the upper body motion constraints, an inverse kinematics simulation was used to pose the model.

After simulation, the discrepancy between the motion part and the red sphere (illustrating the attachment of the motion marker on the body) was studied (Figure 3.8) and the motion marker was moved to the middle of that connecting line. This process was repeated several times such that final simulation had almost no discrepancy between the location of yellow and red spheres in the static pose (Figure 3.9). The markers of the lower body were moved during this process if needed.

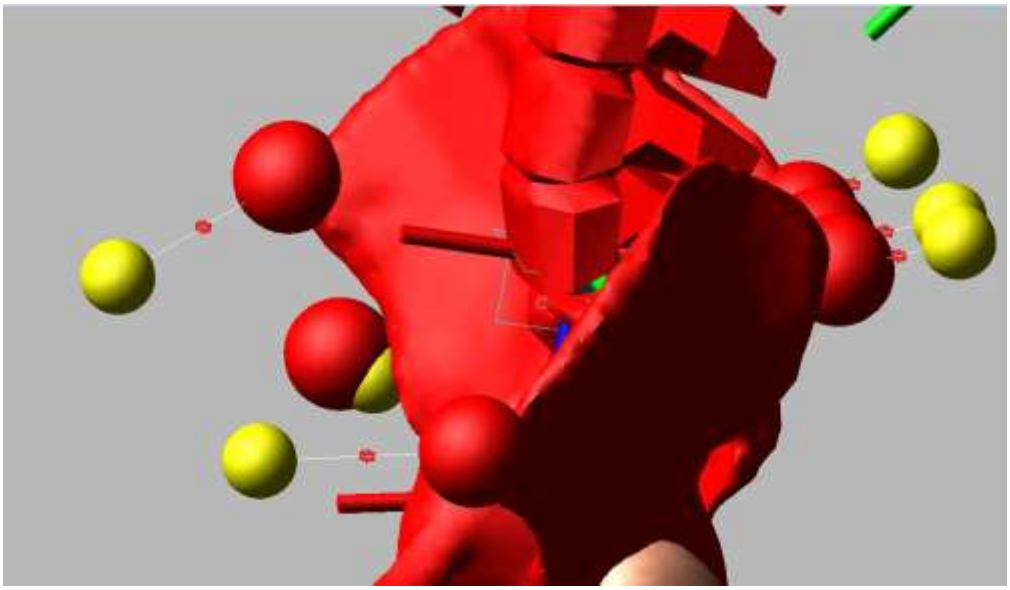

Figure 3.8. In order to adjust the location of motion constraints relative to body segments, the model is simulated into static pose.

The final result of adjusting the motion constrains relative to the body segments is presented in figure. The location of the motion constraints relative to the model was further evaluated in the Inverse Kinematic simulation of the gait.

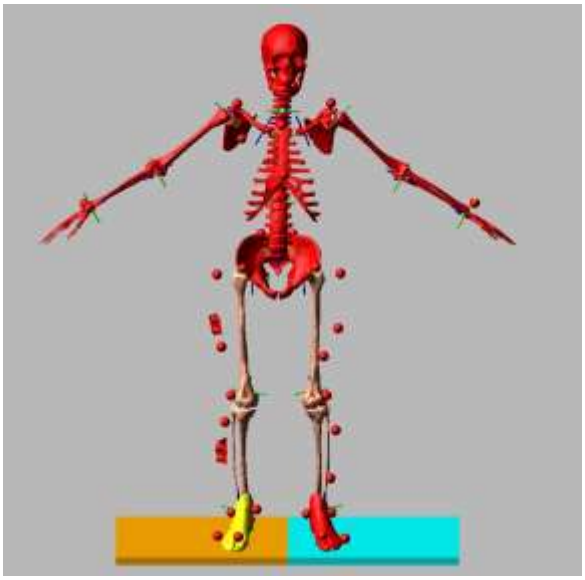

Figure 3.9. There is no discrepancy between location of yellow spheres and red spheres after location of motion constraints are adjusted to the body segments.

Knee Model

The anatomical knee model presented here consists of femoral cartilage attached rigidly to the upper leg segment, medial and lateral tibial cartilage attached to the lower leg segment, major ligaments originating from the upper leg and inserting into the lower leg as discussed in Chapter 2. In addition, the knee model includes the patella and menisci.

Contact force in the Adams environment is calculated based on interpenetration of geometries. In order to study the patellofemoral contact pressure distribution, the patella cartilage was discretized into 3mm x 3mm elements. Each of these small elements was attached to the patella bone via a fixed joint and a contact is defined between each of these elements and the femoral cartilage (Figure 3.10).

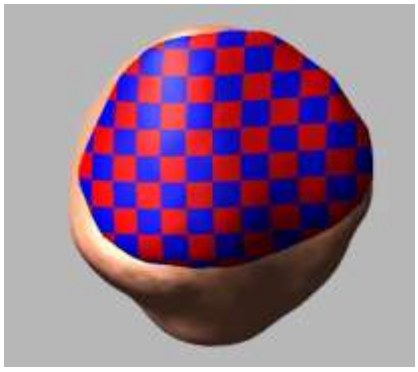

Figure 3.10. The patellar cartilage is divided into 100 3 mm x 3 mm elements.

The contact mechanics between the femur cartilage and patella cartilage as well as contact between tibia and femur was defined based on the study previously described in Chapter 2 (k=327(N/mm) B=5(N s/mm) and n=2.07). Optimizing the contact parameters of a model with menisci by adjusting the predictions of a multi-body model to a FE model yielded the following contact parameters between menisci and cartilage (k=19(N/mm), B=0.1(N s/mm), n=3.37) [Guess et al. 2010].

Medio- lateral stability of the patella was provided by the medial patellofemoral ligament (MPFL) and lateral patellofemoral ligament (LPFL). The patellar tendon was modeled as non-linear springs in parallel with a linear damper connecting the distal side of the Patella part to the lower leg segment on the tibial tubercle (The force prediction model uses equation 2.2). Location of insertion and origin and also mechanical characteristics of the Patellar Tendon, MPFL and LPFL are presented in Appendix 1 in detail.

Four of the muscles were directly attached to the patella (rectus femoris, vastus medialus, vastus lateralus and vastus intermidus). In the inverse kinematic phase of the simulation, 7.5 Newton was put on each of these muscles to hold the patella up.

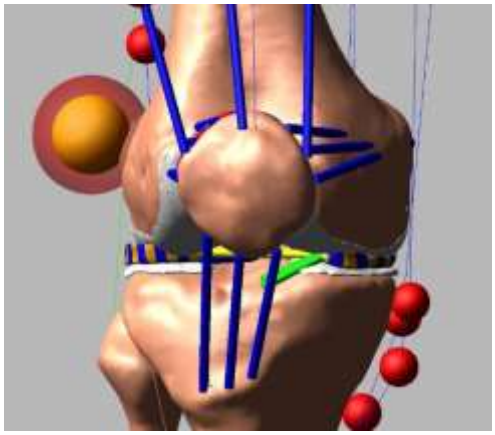

Figure 3.11. The knee model includes discretized menisci.

The Menisci were modeled by dividing the medial and lateral meniscus geometries into several wedge shaped rigid bodies. The sectioned geometries were created by the Boolean intersection of 10 degree wedges with the medial and lateral menisci. The medial and lateral menisci were divided into 19 and 25 parts respectively. The mass and inertia properties as well as center of mass for each menisci part were calculated based on the volume of geometry and average density of 1100 kg/m^3.Each menisci part is

connected to its neighboring part by 6 x 6 stiffness matrices. The stiffness matrix is populated by the result of an optimization study based on reducing the displacement error between a finite element model and multi-body model [Guess et al. 2010].The stiffness matrix is presented in Eq. 3.2.:

$$\begin{bmatrix} F_\theta \\ F_r \\ F_z \\ T_\theta \\ T_r \\ T_z \end{bmatrix} = \begin{bmatrix} K_\theta & K_{\theta r} & K_{\theta z} & 0 & 0 & 0 \\ K_{\theta r} & K_r & K_{rz} & 0 & 0 & 0 \\ K_{\theta z} & K_{rz} & K_z & 0 & 0 & 0 \\ 0 & 0 & 0 & TK_\theta & 0 & 0 \\ 0 & 0 & 0 & 0 & TK_r & 0 \\ 0 & 0 & 0 & 0 & 0 & TK_z \end{bmatrix} \begin{bmatrix} \theta \\ r \\ z \\ a \\ b \\ c \end{bmatrix}$$

Equation 3.2.

WhereF_θ, F_r and F_z are the translational forces and θ, r and z are relative translation between two neighboring parts along circumferential, radial and axial direction of the menisci, respectively. T_θ, T_r *and* T_z are torques and a, b, and c are relative angular displacement about those same axes between two neighboring elements. $K_\theta, K_r, K_z, K_{\theta r}, K_{\theta z}, K_{rz}, TK_\theta, TK_r$ and TK_z are the stiffness matrix parameters which are different for medial and lateral menisci. The horn attachments were modeled as non-linear elastic springs using (Equation 2.2). The zero load length was assumed to be the distance between the origin on tibia and the insertion on the meniscus when the knee was in the MRI position. The stiffness of the horn attachments was determined from the works of Hauch et al. (2010) and is presented in Table3.2 as well as stiffness of other knee ligaments and patellar tendon. The location of the insertion and origin was described by Kohn and Moreno (1995) and Wilmes et al. (2007, 2008) and is discussed further in Appendix 1. Mechanical properties of the anterior intermensical ligament (AIML) were unknown and the value of 200N was chosen as the stiffness. Note that the stiffness of the AIML is an order of magnitude lower than the horn attachment stiffness values. Based on

a cadaver study performed by Poh et al. (2012), the load transfer in the menisci is not dependent on the AIML.

Ligament	Stiffness (N)
Antero Medial - ACL	6200
Postero Lateral – ACL	3400
Antero Lateral - PCL	12500
Postero Medial - PCL	1500
Anterior - LCL	2000
Intermediate - LCL	2000
Posterior - LCL	2000
Anterior Superficial -MCL	2500
Intermediate Superficial - MCL	2600
Posterior Superficial -MCL	2700
Anterior Deep-MCL	1500
Posterior Deep - MCL	1500

Attachment	Stiffness(N)
Lateral Anterior Horn	2810
Lateral Posterior Horn	1269
Medial Anterior Horn	2349
Medial Posterior Horn	1486
Anterior Intermensical ligament	200
Superior MPFL	150
Central MPFL	150
Inferior MPFL	150
Superior LPFL	150
Central LPFL	150
Inferior LPFL	150
Medial Patellar Tendon	3500
Central Patellar Tendon	3500
Lateral Patellar Tendon	3500

Table 3.2. Stiffness of each ligament bundle as well as patellar tendon and meniscal horn attachments has been derived from the literature.

Foot Model

Modeling the interaction of the ground with the foot requires the geometry of the bones and also geometry of surrounding soft tissue. Bone geometries were previously created similar to the bones of the lower and upper leg as discussed in Chapter 2. In order to build the geometry of the surrounding soft tissue around the foot the upper threshold of the images in 3D slicer was increased to 1600, enabling the automatic segmentation tool to capture the entire foot surface. Following the post processing in Geomagic Studio, the foot geometry was divided into 5 rigid bodies.

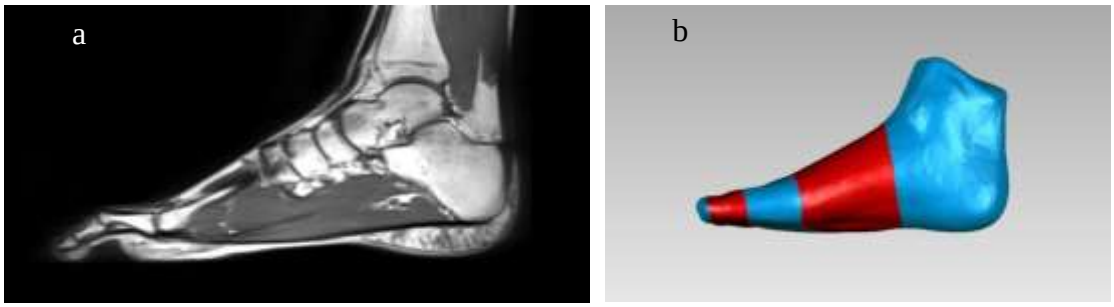

Figure 3.12. The foot's skin has been created by thresholding the MRI (a). The Skin geometry is divided into five segments (b) from left to right; Tip, Toes, Balls of feet, mid foot and Heel.

The Bone geometries were categorized into two groups, toes and foot. A revolute joint between these two parts in parallel with a torsional spring was defined based on the description presented in the literature [Raychoudhury et al. 2014]. The heel and mid-foot section of the skin were attached to the foot bone geometries via bushings while the ball and toe sections of the skin were attached to the toe bone parts via single bushings. However, the tip part of the skin geometry was not attached to the foot and was attached to the toe part of the skin via bushing.

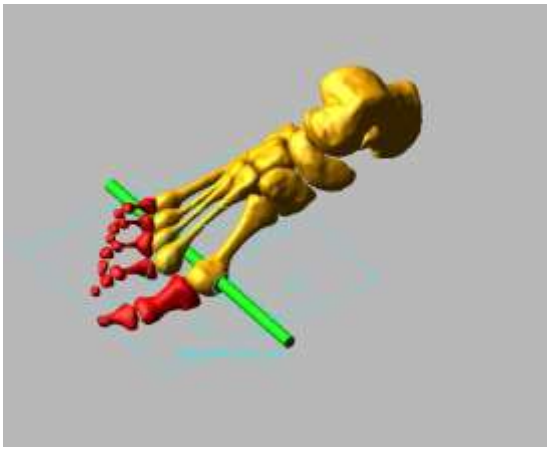

Figure 3.13. A revolute joint connects the two parts of the foot.

The ground reaction force was calculated by combining the same Hertzian contact model with damper discussed in the Chapter 2 [Sharf and Zhang, 20006]. The force exponent is set at 1.5, Damping 0.1 (N s/mm), Penetration depth 0.1 (mm), Static Coefficient 0.8, Dynamic Coefficient 0.7, Stiction Transition Velocity 100 (mm/s) and Friction Transition Velocity at 1000 (mm/s). The stiffness of contact for all parts was set at 50 (N/mm) except from the contact between balls of the feet and the ground which is set at 200 (N/mm) (Nigg et al. 2000).

The ankle joint was modified from a set of three perpendicular revolute joints to two revolute joints with skew axes described by Isman And Inman (1969) to model the

Talocrural (Ankle, Green cylinder) and talocalcaneal (Subtalar, Red cylinder) joints (Figure 3.14).

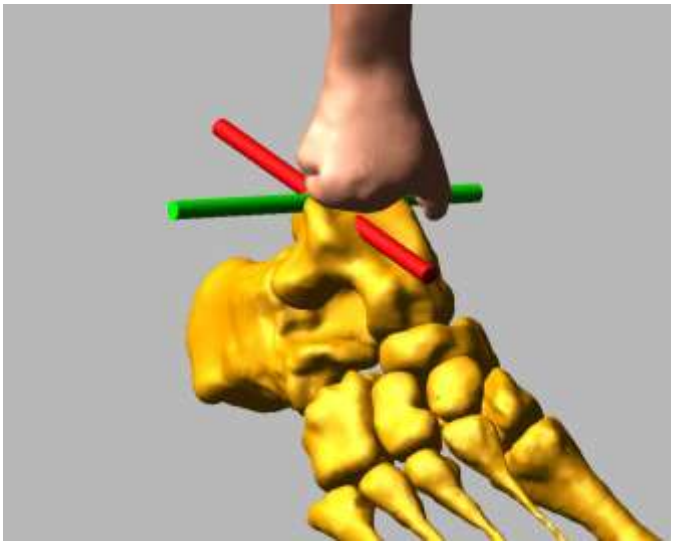

Figure 3.14. Two skew axes revolute joints connect the foot to the lower leg.

Muscle Model

Each muscle-tendon complex was modeled by specifying the geometry and defining a force actuator. The focus of this study is on the legs of the subject and more specifically the knee mechanics. Therefore, only the muscles that cross the right hip, right knee and right ankle were modeled.

To define the geometry, a minimum of two points, origin and insertion, is required. Each point is rigidly attached to a body segment; in this case, lower torso, upper right leg, lower right leg, right foot or right toes. The muscle path is usually defined as a straight line connecting the origin to the insertion of the muscle. However, if a muscle wraps around the bone or is constrained by other muscles, intermediate points called "Via Points" were introduced to define the path. Via points prevent the passing of muscle action lines through the bones or deeper muscles during motion. The location of origins,

insertions and via points were all defined in the segment's reference frame that they were attached to, based on the description by Delp et al. (1990).

The force generating actuator was active only in the forward dynamics portion of simulation and was defined as a feedback PID controller. The PID controller used the length of the muscle as the process variable and compared it to values recorded in the Inverse Kinematic portion of the simulation. PID values for each muscle were defined individually based on the maximum physiological load of the muscle [Arnold et al. 2010]. Maximum physiological force of the muscle was calculated by multiplying the muscle cross sectional area [Ward et al. 2009] to the maximum stress (0.6 MPa) of the muscle (Equation 3.3).

Equation 3.3 $$F_{MAX} = \sigma_{max}.pCSA$$

Whereσ_{max}, the maximum isometric muscle stress and was assumed to be 0.6 N/mm^2 [Li et al. 2007].

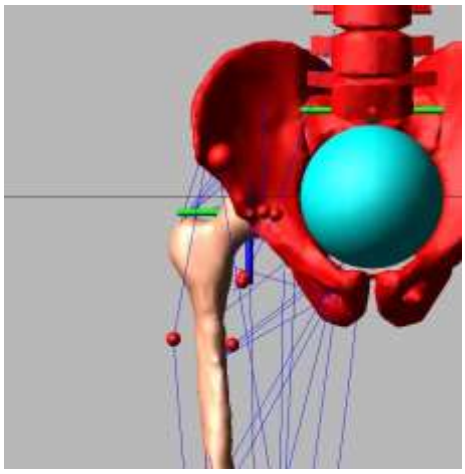

Figure 3.15. Most muscles are modeled as two point force actuators.

Simulation

The simulation consists of two steps, Inverse Kinematics and Forward Dynamics. The input to the modeling scheme is only the motion data captured in the gait lab and the Geometries created from MRI. Therefore, the ground reaction force recorded from the force plates can be used to validate the model.

Inverse Kinematics

In the inverse kinematics phase of the simulation, motion of each reflective marker, recorded in the gait lab, was used to move the body segments as they were constrained by the joints, knee contact and ligament forces and contact forces between the foot geometries and the ground. Each motion part (yellow sphere in Figure 3.7) was attached to the body segments via bushings and the bushings define the location of each body segment in the space during the simulation.

A 7.5 N force was also applied to the quad muscles force actuators (vastus medialus, vastus lataralis, vastus intermidius and rectus femoris) in order to hold the patella in place during the simulation.

The inverse kinematics portion of the simulation was performed to measure the joint angles and muscle lengths during gait (The output of the model). Length of the muscles that included via points, were calculated by adding the length of each existing part.

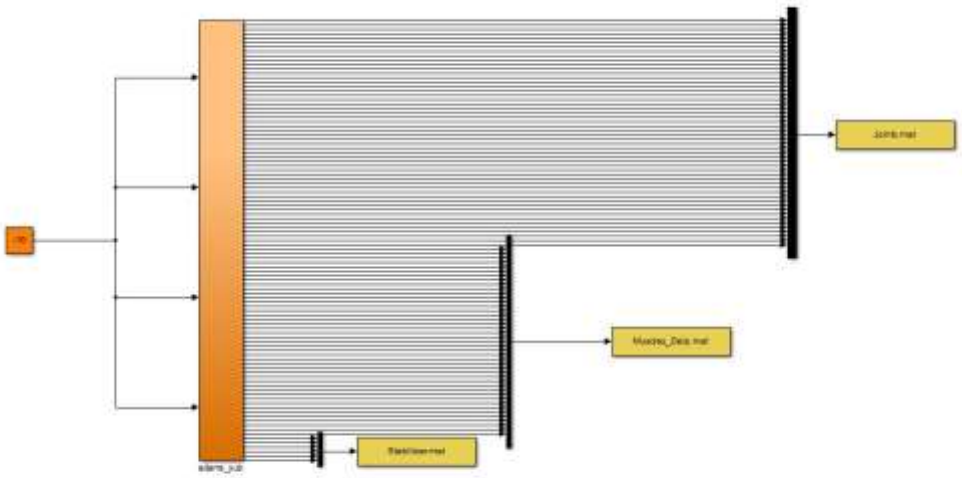

Figure 3.16. Inverse kinematic plant in Simulink.

The simulation was 5 seconds long and took about 10 minutes of processing time on a machine with Intel Core i7-4770@3.40 GHz with 16.0 GB of RAM. The step sizes were 0.005 seconds and the number of communications of Simulink and Adams per output step was set at 1.

Forward Dynamics

After the motion constrains were deactivated, in the Forward Dynamics portion of the simulation, feedback control loops were used to generate muscle forces (43 muscles) acting on the right leg as well as torques acting on the joints of remaining body segments (15 spherical joints and 1 revolute joint for the left toes part). Thus, the right leg was muscle-driven.

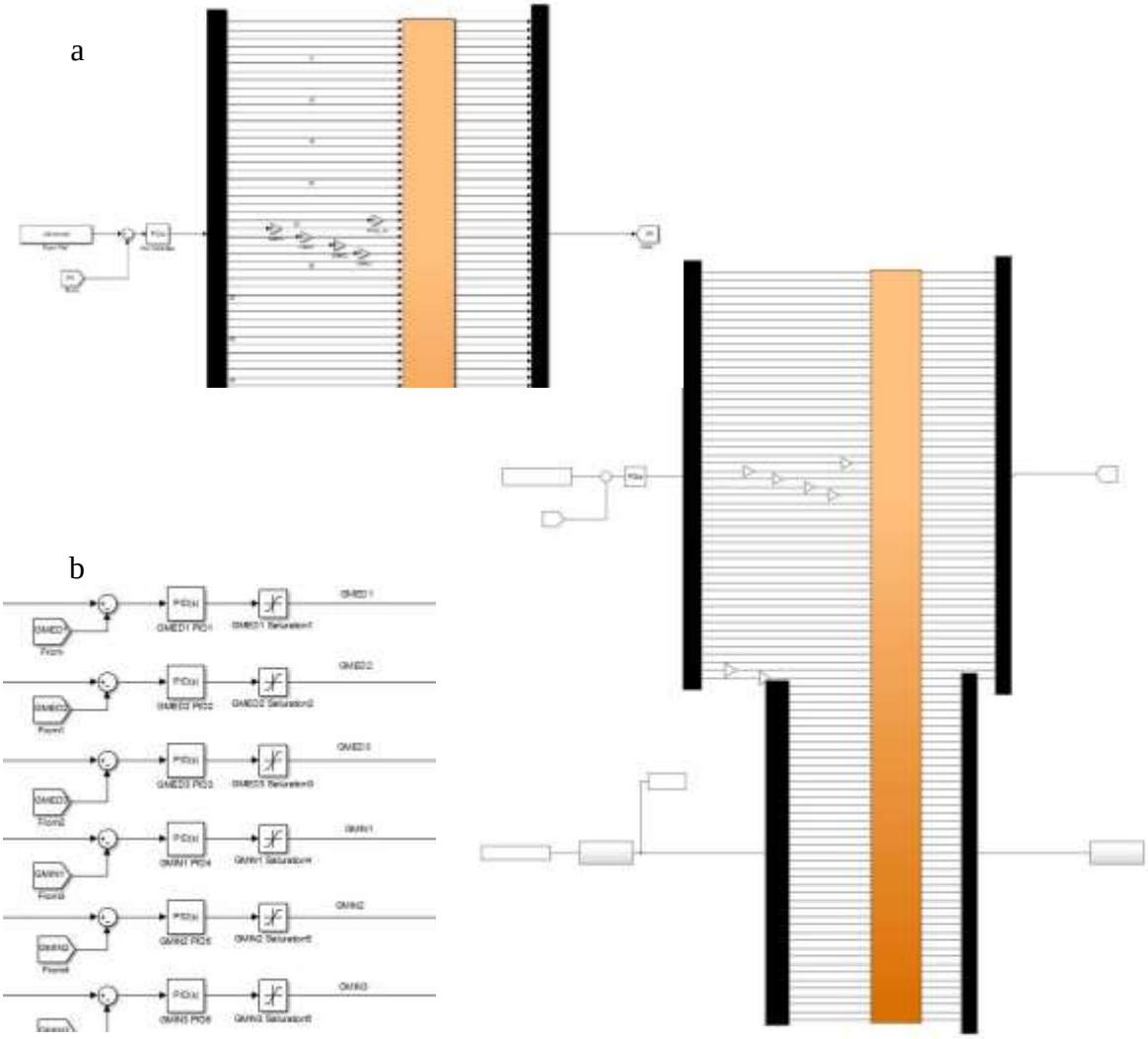

Figure 3.17. Forward Dynamics plant in Simulink. The joints use the same PID controller (a) while the muscles use individualized PID values (b) that are derived from PCSA.

The force actuator controllers and torque actuator controllers were designed to reproduce the muscle lengths and joint angles recorded during the Inverse kinematic phase respectively. Target length of each muscle was defined as the length of the muscle during the Inverse Kinematic and the difference between the target length and the current length of the muscle at each step was defined as the error signal. The same control scheme was used to calculate the torques acting on the body segments by the torque actuators of each revolute joint. The difference between the joint angles around each axis with the corresponding recorded value in the inverse kinematics was defined as the error signal and a PID controller was used to produce the torque based on the error signal.

Computational Study

The current study looks at two different biomechanical functions of the knee:

1. The contact pressure distribution of the patellofemoral joint with three pathological conditions was compared to the normal knee. The Abnormalities studied were Patella Alta (high patella riding), Patella Baja (low lying patella) and a knee with tibial tuberosity-trochlear groove (TT-TG) distance of more than 20 mm (High TT-TG values leads to patellar instability).

2. The biomechanics of the meniscus in response to horn attachment stiffness modification was examined.

In order to study the contact pressure distribution of the patellofemoral joint, four different models were developed from using the method previously described. MRI measurements were used to determine the TT-TG distance (12 mm) and the Caton-Deschamps index (1.09) of the subject's right knee.

1. **Normal** Model: The original model based on the MRI measurements, insertion and origin location.
2. **TT-TG** Model: TT-TG of the model is increased by moving the Patellar tendon insertion points Tibial Tuberosity 8 mm laterally to model the pathological case of TT-TG distance of 20 mm.

3. **Patella Alta** Model: Caton-Deschamps index value was increased to 1.2 by increasing patellar tendon length
4. **Patella Baja** Model: Caton-Deschamps index value was decreased to 0.8 by decreasing patellar tendon length

In order to study the biomechanics of the menisci, five different models were created by modifying the laxity of horn attachments. The zero-load length was set of each attachment was set at 80%, 90%, 100%, 110% and 120% of the MRI measured distance.

Results

The ground reaction forces in Vertical, Anterior-Posterior and Medial-Lateral directions recorded from the force plate and compared to the predicted ground reaction force in the Normal Model (Fig. 3.18) The predicted forces were acceptable for most of the gait cycle except for the toe-off phase.

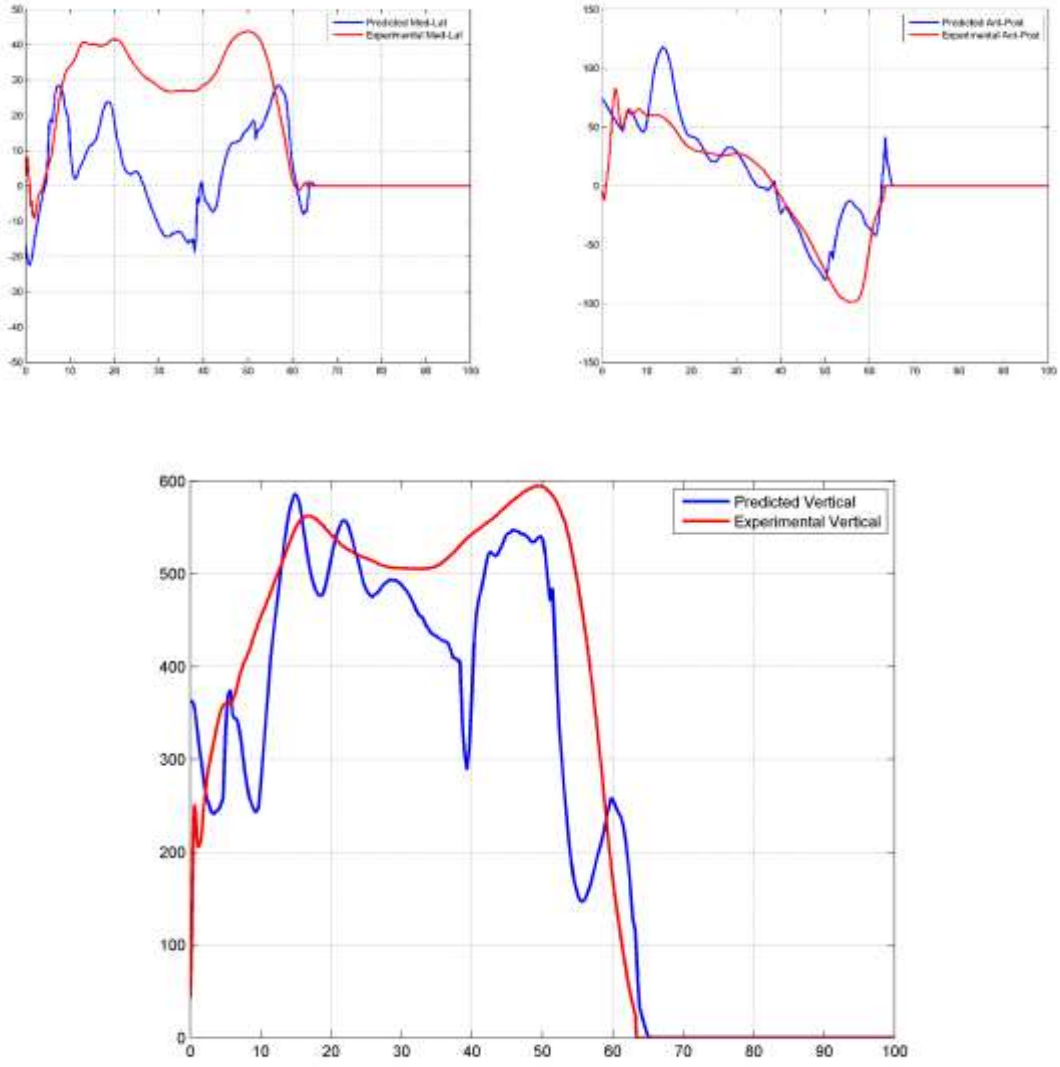

Figure 3.18. The predicted ground reaction force is compared against the experimental ground reaction forces in all directions.

The goal of Forward Dynamics simulation is to track the motion recorded during the Inverse kinematics simulation. Comparing the joint angles between these two simulations gives us a good understanding of the accuracy of the model. All of the joints in the body are driven by torque actuators except right hip, knee and ankle. In The joints with active torque actuators, the torque acting on the joints is calculated by joint angle PID controllers. Angles in the Inverse Kinematics match those of the Forward Dynamics model and comparison is not required. However, the torques acting on the Right Hip, Right Knee and Right Ankle are produced from the muscle force actuators. Therefore there may be a discrepancy between those angles. A comparison between the joint angles in inverse kinematics and forward dynamics is presented in figures 3.19, 3.20 and 3.21 for ankle, knee and hip respectively.

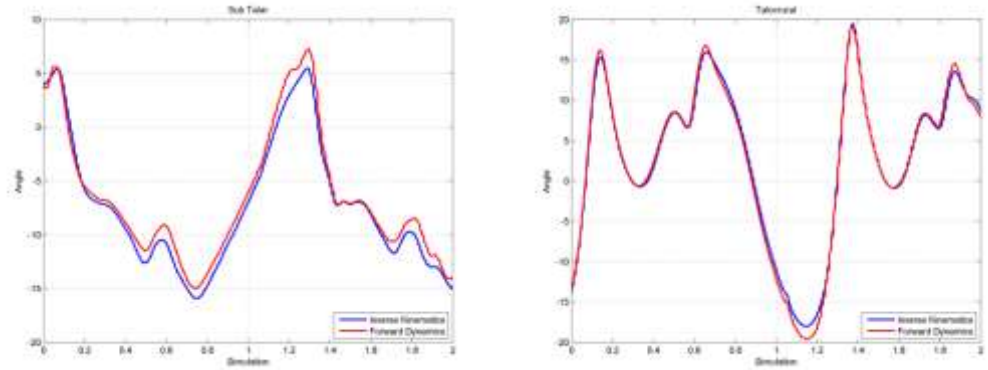

Figure 3.19. Comparison of ankle angles between Inverse Kinematics and Forward Dynamics.

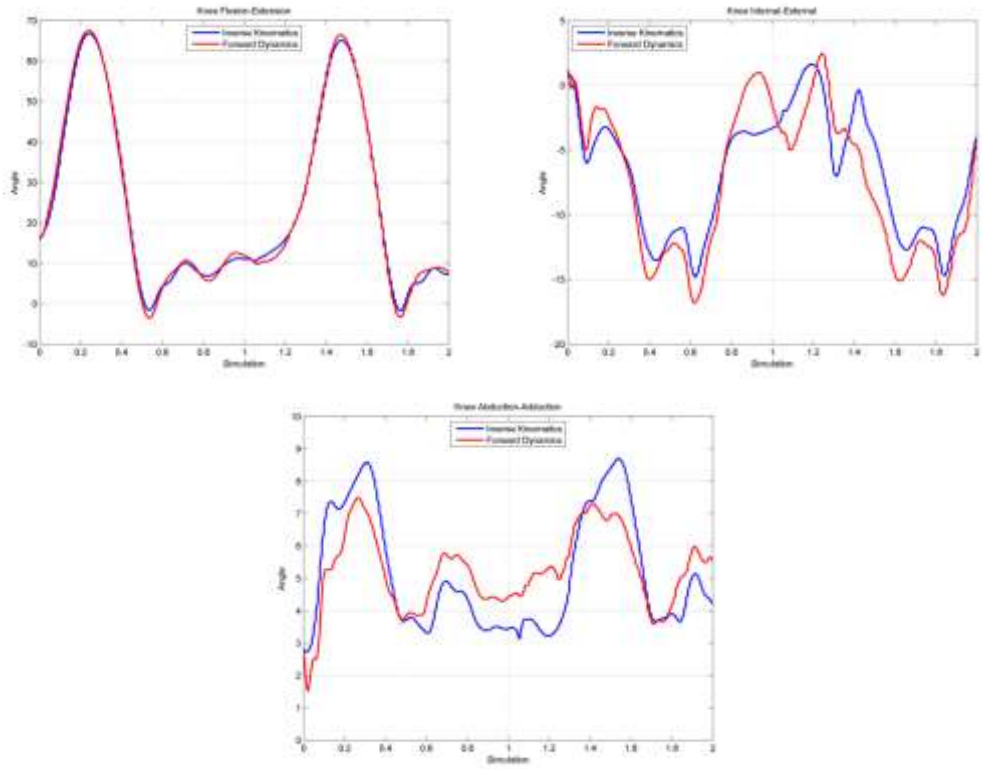

Figure 3.20. Comparison of knee angles between Inverse Kinematics and Forward Dynamics.

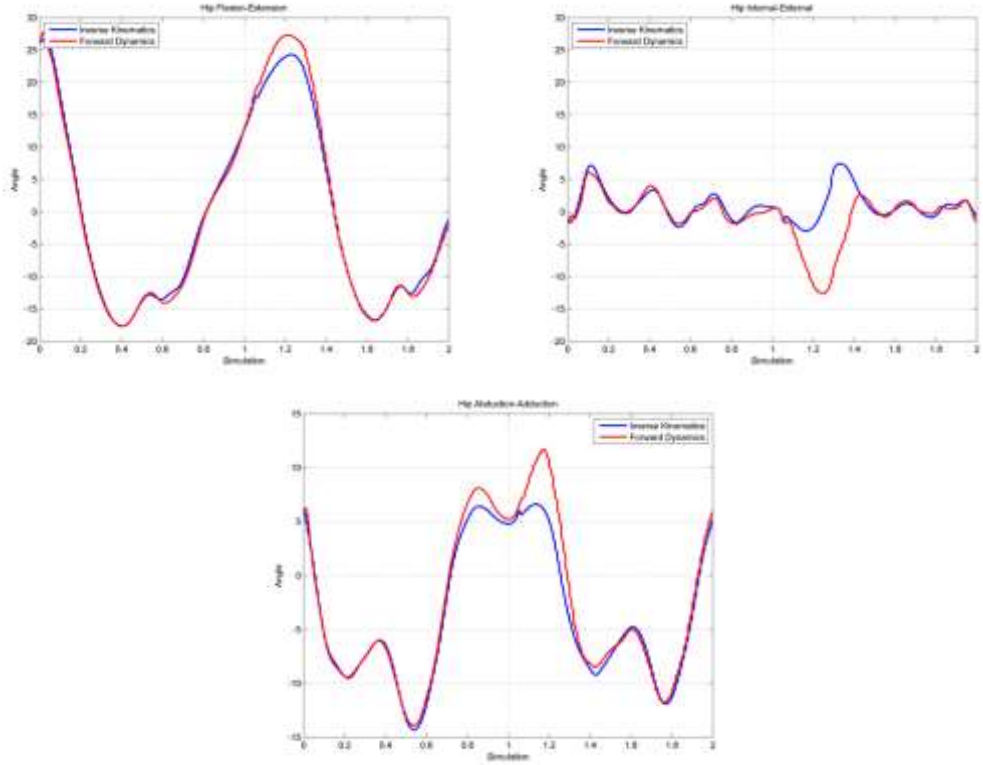

Figure 3.21. Comparison of Hip angles between Inverse Kinematics and Forward Dynamics.

The predicted contact forces between femoral cartilage and medial and lateral cartilage during the same gait cycle is presented in Figure 3.22. The predicted ground reaction force in the vertical direction is presented for comparison purposes.

Figure 3.22. Sum of forces acting on the medial tibial cartilage are larger than sum of the forces acting on the lateral tibial cartilage.

The ratio of the contact load that is taken directly by the tibial cartilage from the femoral cartilage to the load transferred through the menisci is an important consideration. This ratio is presented for both lateral and medial tibial cartilages (Figure 3.22). A ratio of 0 would demonstrate that all of the femoral contact force is taken by the meniscus and as opposed to a ratio of 1 which indicates that all the femoral contact force is taken directly by the tibial cartilage. The medial meniscus has a lower ratio during early phases of the gait compared to lateral meniscus, indicating a bigger portion of the load passing through the meniscus in the medial compartment. There is also a minimum at 60% and 90% of the gait cycle in the medial side. However, the lateral compartment has a lower ratio in the swing phase of the gait.

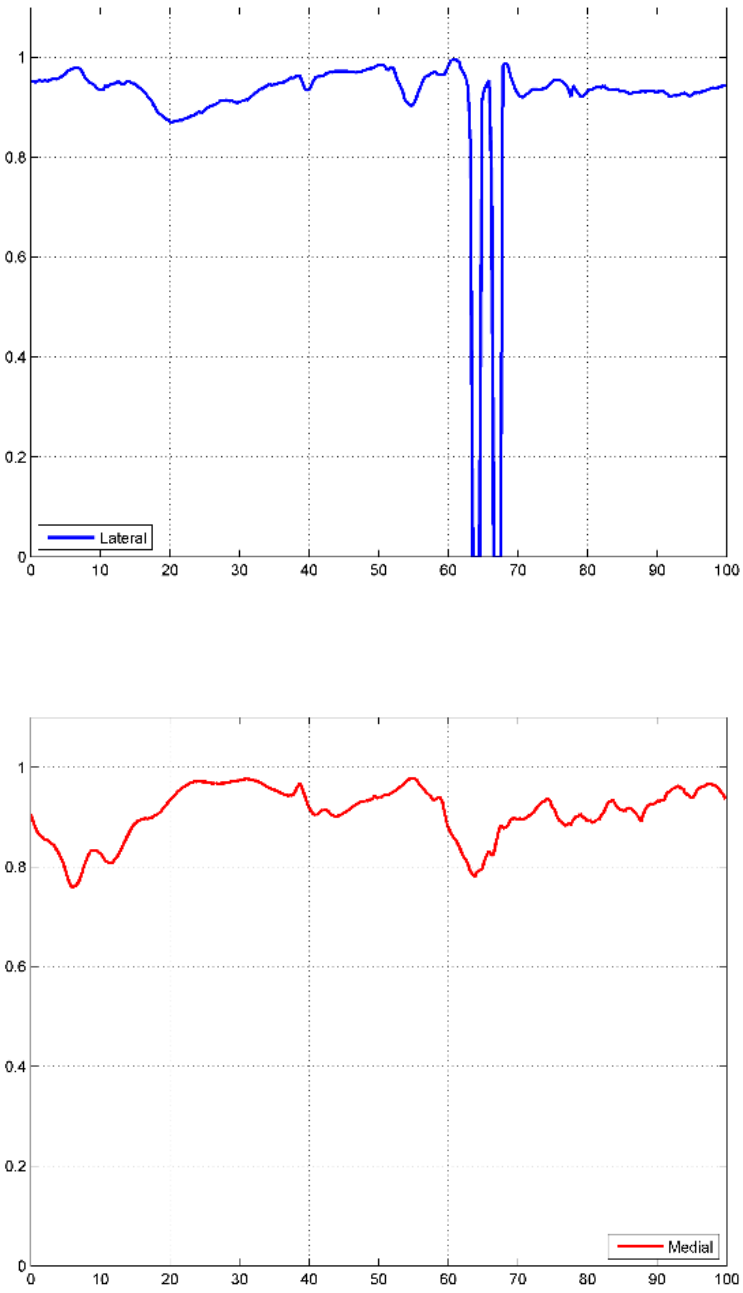

Figure 3.23. The ratio of the load that is passed directly from femoral cartilage to tibial cartilage is changing throughout gait.

Patellofemoral Contact Mechanics

There was no significant difference between the predicted ground reaction forces of the four models. The ground reaction force is shown in Figure 3.24 over the gait cycle.

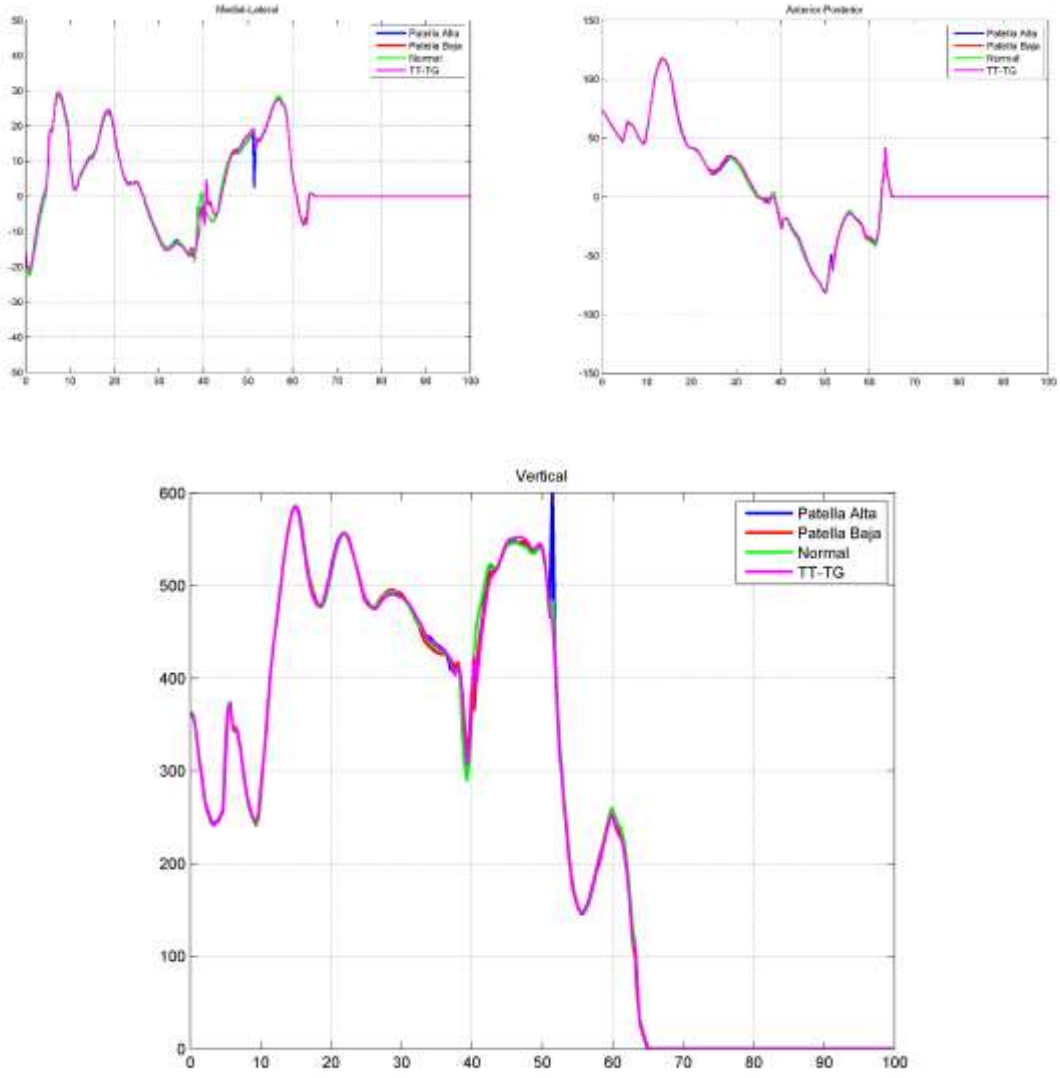

Figure 3.24. The predicted ground reaction force is similar between the four models.

Due to the fact that the only active force acting on the patella comes from the quad muscle group (vastus medialus, vastus lateralis, vastus intermidius and rectus femoris), the contact mechanics of the patellofemoral joint were studied during the loading phase of the gait cycle (approximately 30% of the gait cycle) at which vasti activation was maximum (Figure 3.25).

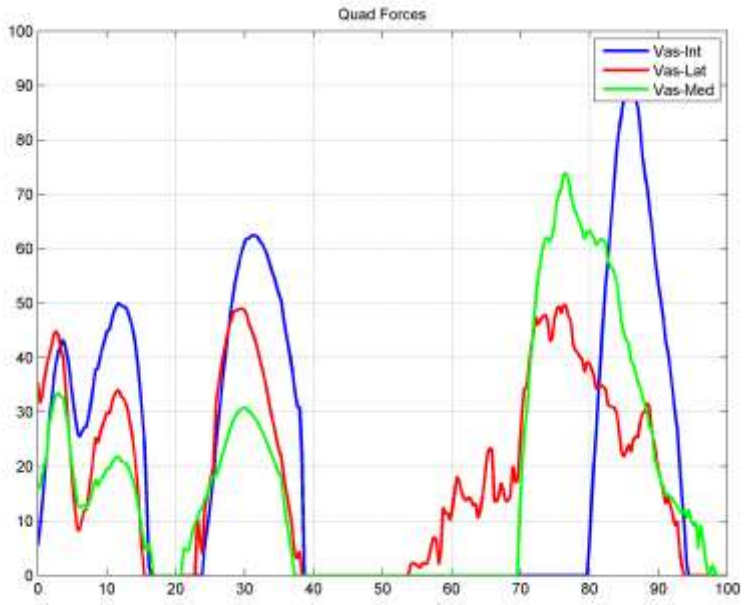

Figure 3.25. 30% gait phase is chosen to study the patellofemoral pressure distribution.

The Contact area at the loading phase of the Normal model was predicted to be 225 mm^2. The contact area prediction was lower in the Patella Alta and TT-TG model, 162 mm^2 and 189 mm^2, respectively. However the contact area prediction in the Patella Baja model was higher than the Normal model at 324 mm^2.

The maximum contact pressure in the Normal model was 2.2 MPa. Patella Alta and TT-TG model predicted higher Maximum Contact Pressures at 3 MPa and 2.7 MPa respectively. However the Patella Baja model predicted lower pressure compared to the Normal model at 1.7 MPa. The decline in the contact area between patellar and femoral

cartilage led to an increase in the maximum contact pressure in the Patella Alta and TT-TG model compared to the Normal model while the Patella Baja had a lower maximum contact pressure compared to the Normal model due to higher contact area.

The changes of the average contact pressure between the models were similar to the maximum contact pressure. The Normal model had an average of 0.49 MPa contact pressure over the entire patella, while this average was 0.61 MPa, 0.7 MPa and 0.29 MPa for the Patella Alta, TT-TG and Patella Baja models respectively.

A contour of pressure distribution at the loading phase of the gait (30%) is shown for the Normal model and the TT-TG model in Figure 3.26. The pressure area has moved laterally in the TT-TG model and the force is taken by smaller area on the lateral side of the patellar cartilage.

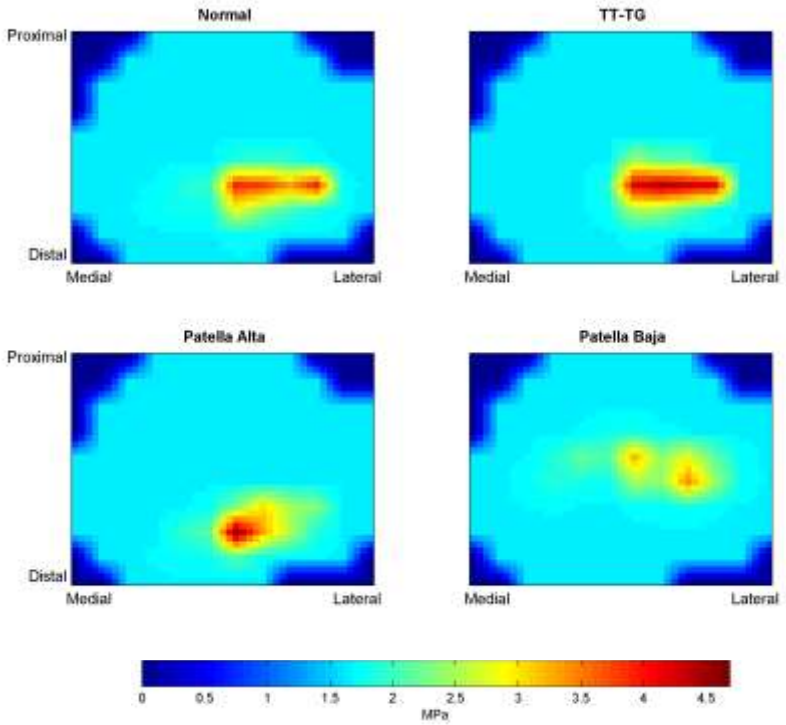

Figure 3.26. The patellar contact pressure in the TT-TG model is moved laterally in the TT-TG Model, distally in patella Alta and proximally in the Patella Baja, relative to the Normal Model.

A contour of pressure distribution during the loading phase of the gait (30%) is presented for Normal, Patella Alta and Patella Baja models in Figure 3.26. The contact area of the patella alta model has moved distally as the patella was riding high in the femoral cartilage groove, limiting the contact area to a small portion of the patella, thus increasing the maximum contact and average contact relative to the normal model. However, in the patella baja model, the patella was pulled by the patellar tendon making a bigger area available for the contact and therefore decreasing the maximum pressure and average model and some of the patella cartilage that take no load during the loading phase of the gait, now are under compression.

The contact parameters of the patellofemoral joint are summarized in Table 3.3.

Model	Contact Area (mm^2)	Maximum Contact Pressure (MPa)	Average Contact Pressure (MPa)
Patella Alta	162	3	0.61
Patella Baja	324	1.7	0.29
Normal Model	225	2.2	0.49
TT-TG Model	189	2.7	0.70

Table 3.3. The contact area in the PF joint is increased in the Patella Baja model and decreased in the Patella Alta and TT-TG Model compared to the Normal Model.

The Effect of Horn Attachment Laxity on the Meniscal Extrusion

Four models were created to be compared against the menisci biomechanics of the Normal model. The zero load length of the horn attachments in those models was set at 80%, 90%, 110% and 120% of the values in the Normal model (zero load lengths of the horn attachments in the Normal model was set at values measured from the MRI).

The motion of the meniscus to the tibial cartilage affects the ratio of the load transfer through the meniscus to the total contact load transferred through the knee. Two variables were used to examine this motion; the extrusion of meniscus which quantifies the portion of the meniscus that is not on the tibial cartilage, and the meniscal excursion which quantifies the anterior-posterior motion of the meniscus.

The meniscus is considered extruded when it extends beyond the tibial cartilage. Meniscal extrusion was measured by guidelines provided by Hunter et al. (2006). First, the MRI slice in which the medial spine of tibia had the greatest area was selected (mid-Coronal slice). Tibial plateau, medial tibial plateau, lateral tibia plateau width, and also meniscal coronal width and meniscal extrusion was measured for both medial and lateral meniscus.

The meniscal body extrusion index, which is independent of the knee size, was measured to be 2.6 and 2.3 in medial and lateral meniscus respectively.

Predicted ground reaction force of a gait cycle is presented (Figure 3.27) in all of the five models. The GRF predictions are almost identical between models.

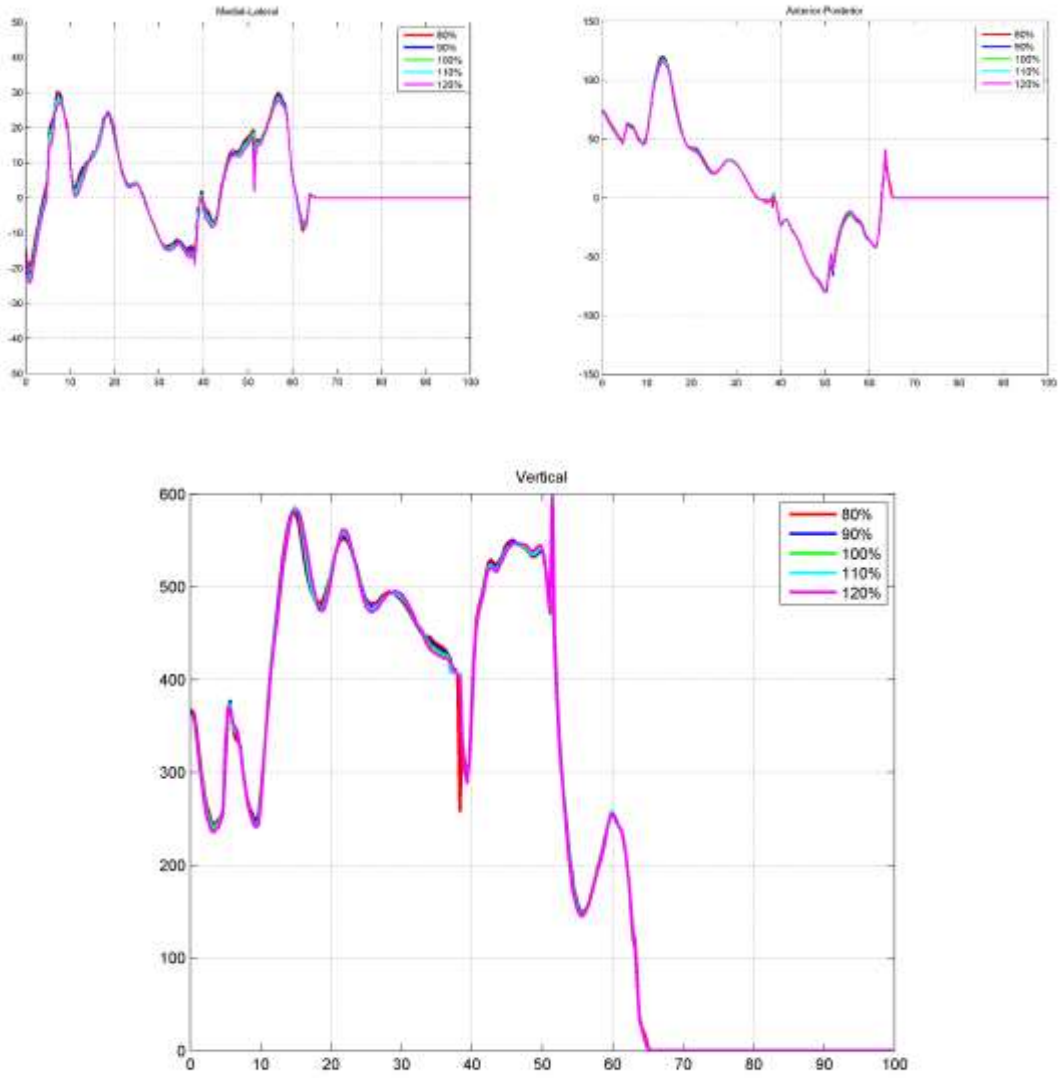

Figure 3.27. The predicted ground reaction force is similar between the five models.

The proportion of contact force that is transferred from the femoral cartilage to the tibial cartilage to the total tibio-menisco-femoral contact force is plotted for all the five models in both the femoral and medial compartments of the knee (Figure 3.28). The changes of the ratio during the gait is similar in all the models, with ratio decreasing as the horn attachments become lax, allowing the menisci to move towards the outside of the knee. Therefore, more of the load is being transferred through the tibio-femoral contact.

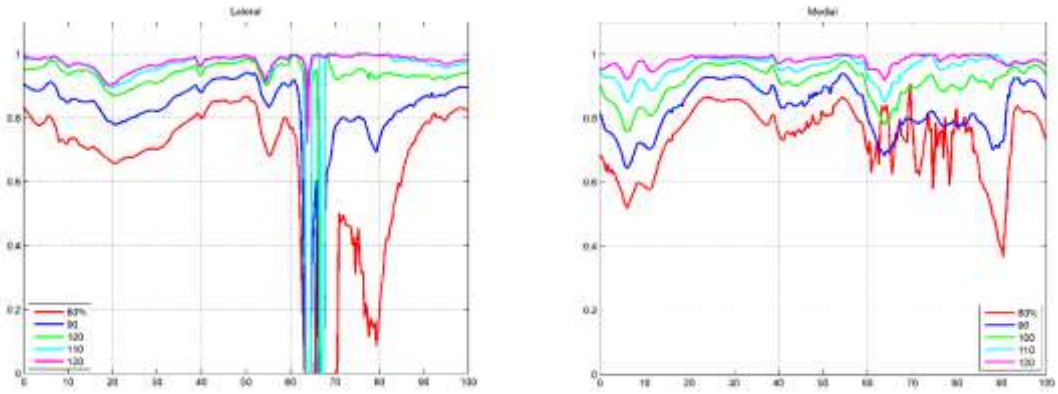

Figure 3.28. Ratio of the force transmitted directly from femoral cartilage to tibial cartilage to the total force that is transmitted through the knee. Higher portion of the force is transmitted through the menisci as the zero load length of horn attachments become shorter.

In order to measure the meniscal excursion, a local coordinate system was defined and is shown in Figure 3.29 [Grood and Suntay 1983]. The excursion distance over the gait cycle was measured to be 9.2 mm and 6.4 mm in the anterio-posterior direction for medial and lateral meniscus respectively. The anterior-posterior excursion of the medial side of the medial meniscus is greater than the lateral side of the lateral meniscus in the normal model.

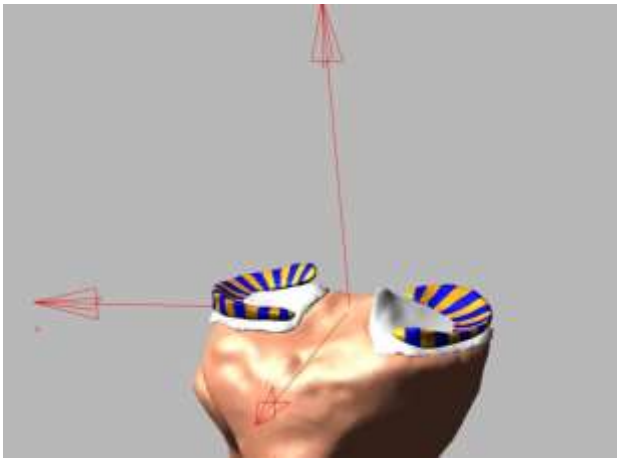

Figure 3.29. Tibial Coordinate system is used to measure the excursion of the menisci.

In order to measure the meniscal extrusion in the model, the distance between the outer edge of the most medial element of the medial meniscus and the outer edge of the

medial meniscus along the medial-lateral axis of the Grood and Suntay (1983) tibia coordinate, and the distance between the outer edge of the most lateral element of the lateral meniscus and the outer edge of the lateral meniscus along the same axis was defined as the meniscal extrusion for medial and lateral meniscus respectively.

Meniscal extrusion was measured at 90% of the gait cycle where the knee was close to the MRI angle and the leg was loaded less during the swing phase. Meniscal extrusion at 90% of the gait cycle (Swing Phase) was measured for all of the models and is presented in Table 3.4. As laxity of the horn attachments increases, Meniscal extrusion increases.

Horn attachment length percentage	Medial Meniscus (mm)	Lateral Meniscus (mm)
80	0.5	-1.7
90	0.9	-1.2
100	2.2	0.3
110	3.8	0.8
120	4.4	1.9

Table 3.4. Extrusion distance of the medial and lateral meniscus at 90% of the gait cycle (Swing Phase) is increased as the zero load length of horn attachments increases.

Discussion

The motivation for this work was to develop a dynamic multi-body model of the human body with the ability to perform ambulatory activities using Forward Dynamics to calculate knee contact forces and pressure distribution as well as ligament forces. The current study examined the contact pressure distribution in the patellofemoral joint as well as meniscus biomechanics.

Patellofemoral Contact Pressure

The study maps out the pressure distribution of the patellofemoral joint during the gait cycle in a normal knee as well as three pathological cases. The results predict that changes of patellar tendon length and also location of patellar insertion point (tibial tuberosity) leads to significant changes in loading of the patellofemoral joint. The contact area and the peak pressure in the joint are affected.

This study predicted patellofemoral joint stress by finding the force on the 3 mm x 3 mm elements of the patellar cartilage and dividing the force by the 9 mm^2 area. The contact mechanics of the patellofemoral joint was examined at about 30% of gait cycle, where maximum quad muscles forces were predicted. The peak total compressive force on the patellar cartilage was 182 N in the normal model during gait and the maximum pressure was 2.2 MPa in the Normal Model.

In a cadaveric study performed on 7 knees, Upadhyay et al. (2005) studied the effect of patellar tendon shortening (10%) on the PF joint mechanics (Patella Baja). At 15° of flexion, the contact area increased by 18% in the Patella baja knee. In our study, the contact area was examined at the loading phase of the gait (10° of flexion) and the area was predicted to increase by 44% in the Patella Baja model. The difference between these

changes may be attributed at the different flexion angles of the experimental study and the model and also different patellar tendon shortening value (27% in our model).

Another cadaveric study performed by D'Agusta et al. (1993) examined the contact area and the contact pressure at different knee flexion angles. The average contact area was 160 mm^2. At the loading phase, the contact was predicted to be 225 mm^2 in the Normal model. A cadaver study performed by Goudakos et al. (2010) found a range of 275 mm^2 to 400 mm^2 by measuring the pressure film contact area placed inside the joint.

Beseier et al. (2005) estimated a range of 350 mm^2 to 500 mm^2 during a static loaded situation and from 250 mm^2 to 400 mm^2 for female subjects in a computational model.

It should be noted that the contact between patellar tendon and the femoral cartilage (tendofemoral contact) is not defined in our model. According to Huberti and Hayes (1984) the tendofemoral contact supports as much as up to half of the total patellofemoral joint contact force. Meyer et al. (1997) studied the biomechanics of the patella infera (patella baja) and observed that the tendofemoral contact supports up to 80% of the contact force. However, this contact does not affect the biomechanics of the knee until deep flexion angles that are not examined in this study. Therefore, the simplification is acceptable.

Other contact prediction methods such as elastic foundation theory (also known as bed of springs) may be used instead of Hertzian contact theory to enhance the prediction of tiobiofemoral as well as patellofemoral contact prediction. Bei & Fregly (2004) as well as Blankevoort et al. (1991) have used such methods in their models. More sophisticated methods should be incorporated in the future work especially if the goal of the computational study is to examine the joint contact pressure.

In future works the pressure distribution map can be compared to the progression of cartilage deterioration in patients with patella Alta and patella Baja. The comparison enables us to study the effect of pressure changes on the cartilage deterioration observed in patella Alta and patella Baja cases. Since changes of the physiological loads (incline and decline) on the cartilage leads to the deterioration of the articular cartilage, effect of the changes in the mechanical loading (both increase and decrease of the pressure on the cartilage) should be studied extensively.

Menisci Biomechanics

Previous computational and experimental studies suggest that the meniscus plays an important role in the knee contact forces. Thus modeling the menisci in a computational musculoskeletal model that looks into the biomechanics of the knee is necessary. In addition to reducing the articular cartilage contact pressure by increasing the contact area, menisci play an important role in joint stability, load transmission and lubrication. Biomechanics of the meniscus has been studied only in specific loading scenarios and not during ambulatory activities in previous computational models [Danso et al. 2015]. The biomechanical function of the meniscus in our model is a function of horn attachments (stiffness, insertion and origin) as well as geometry of menisci and the matrix stiffness between the elements of each meniscus. The current study was focused on the laxity of horn attachments. Our findings indicate that changes in the length of the horn attachments (±10% and ±20% of the original length) results in changes in the magnitude of forces that are transmitted through each meniscus.

The excursion of the menisci during a walking cycle was 9.2 mm and 6.4 mm for the medial and lateral meniscus respectively. The same method conducted on a different

subject by other researchers resulted in values 13.1 mm and 8.7 mm respectively. The other subject was taller than the subject in the present study and had a bigger build.

There is anatomical evidence that the deep upper oblique portion of the MCL is attached to the medial meniscus [Wagner 1976] However, in a tensile test, the deep bundle of the MCL was weaker than the superficial and the posteromedial capsule [Robinson et al. 2005]. In a cadaveric study, Stein et al. (2011) concluded that the stability of the medial meniscus is not dependent on the medial collateral ligament under compression loading. The deep bundle of the MCL was modeled as DMCL in our model, however the attachment to the menisci was not modeled and should be covered in future models.

The comparison between lateral and medial knee contact force Figure 3.22 reveals that the medial compartment of the knee joint is experiencing larger forces compared to the lateral compartment. This difference may explain why OA occurs more often in the medial side of the knee joint than the lateral side.

The force in the horn attachments are predicted by the same piecewise function as the ligaments in equation. However, the zero-load lengths are assumed to be the length of the bundle in the MRI position. It is possible that the attachments are under tension during the MRI and the actual zero-load length is shorter than the values we used in the model. Therefore, our assumption that the zero-load lengths in the bundles of horn attachments are equal to the length in the MRI is inaccurate. Moreover, the horns are assumed to be straight lines connecting the menisci to the tibia and the wrapping is not modeled.

A meniscus is regarded as “extruded” when it expands beyond the cartilage of the tibia. Disruption of the collagen fibers of the meniscus leads to meniscal extrusion, which

in turn reduces the hoop strength. It might be associated with the presence of OA [Adams et al. 1999]. Medial meniscus extrusion more than 3mm is associated with problems such as degeneration of the meniscus, extensive tear, complex tear, large radial tear, and tear involving the meniscal root. Due to the fact that medial compartment of the knee carries more weight, meniscal extrusion is more significant on the medial side and also abnormalities in the medial compartment of the knee are more frequent than the lateral [Costa et al. 2004]. A cohort study performed Bruns et al. (2014) on meniscal extrusion found that average meniscus extrusion was 2.6±1.4 and 0.9±1.1 for medial and lateral meniscus respectively. The extrusion of medial meniscus was within one standard deviation of the average measurements but the extrusion of lateral meniscus was outside of one standard deviation of the average.

The simulation time was significantly different between the five models ranging from 16 minutes in the 120% model to 73 minutes in the 80% model. The reason for this difference is the larger penetration of menisci element geometries into the femoral and tibial cartilage in the latter model. The contact algorithm in MSc Adams is affected by the geometry penetration and solving a simulation with more penetration, takes a longer time.

General Considerations

Muscle force prediction is a subject of ongoing research. In a multi-body musculoskeletal simulation of human motion, the number of unknown variables (joint torques and muscle forces) is more than the number of equations (degrees of freedom of the system), making it an underdetermined system. Therefore, an infinite number of solutions are available for this system. The solution that is picked up by the muscle force

prediction scheme is dependable on the scheme itself and the parameters involved (P, I and D of the muscle controllers in our study).

It should be noted that predicted muscle forces were derived by comparing the length of the muscle with the recorded length during the Inverse Kinematic phase of the simulation. Thus, it is efficient in predicting forces of the muscles that are shortening. However, modeling the contraction of antagonistic muscle groups during gait is not feasible (situations that the muscles are lengthening and still carry load called eccentric contraction) in our model.

Significant improvement can be made to the muscle force prediction scheme by incorporating more complex models of force prediction. The shortcomings of this method can be improved by combining this method with other methods. For example, a feed forward signal calculated from a Hill muscle model by using EMG signal of the muscles can be used as a secondary signal that is added to the feedback signal calculated by the PID controllers (feedback signal). Adding a feed forward signal enables the muscles to predict the isometric and eccentric contractions that a simple PID controller is not able to predict. But the EMG data is limited and EMG signal can be recorded for only a few surface muscle groups (8 in our study). Moreover, in order to use an EMG signal to calculate the muscle force, EMG signal should be normalized to the Maximum Voluntary contraction (MVC) value. There could be errors in measuring the MVC. For example, lack of training in a specific muscle group may cause a lower MVC value to be reported. Therefore, the MCV trials should be performed under extensive care.

Most of the muscle prediction schemes use the hill-muscle model. However, the activation signal that is used by the Hill muscle model is derived differently. The most

basic Hill model uses the EMG signal as the activation signal. It is also common to calculate the moment required to move the model in an Inverse Dynamics simulation. Therefore, at each flexion angle, based on the moment arm (the perpendicular distance between line of action and joint center), the force can be calculated. The calculated force may be used as a feedforward signal in the Forward Dynamics simulation.

Chapter 4

Conclusion

This study developed a muscle driven forward dynamics simulation of a computational model using subject specific geometries of the lower limb. The model predicts the muscle forces during the gait as well as ligament forces and knee joint contact mechanics including the menisci. This model has the potential to become a powerful tool for orthopedic surgeons in planning surgeries and also predicting injuries. Moreover, the pressure distribution data on menisci and cartilage may prove to be useful in tissue engineering of cartilage and menisci.

The objective of this study was to demonstrate the ability of the concurrent simulation in a subject specific multi-body model to predict the knee mechanics loading. The model is efficient in predicting the tibio-menisco-femoral and patella-femoral contact mechanics as well ligament forces during ambulatory activities.

There are several limitations to the current study. For example, only the right leg geometries were constructed for modeling purposes and the left leg geometries were mirrored. Moreover it was assumed that left knee was an engineering spherical joint (like the rest of the joints in the model). There is a significant difference between the predicted ground reaction forces of right foot and left foot especially in the toe-off region. However, the experimentally recorded ground reaction force was not significantly different. This asymmetry may be caused by the difference between the degrees of freedom (3 degrees of freedom for the left knee compared to 6 degrees of freedom for the right knee) in the model.

The contact forces in the joint as well as the tensile force carried by the ligament are dependent on the active forces of the muscles crossing that joint. Another limitation of this model is the inability to predict the co-contraction of the muscles during the ambulatory movements. A feed forward muscle prediction scheme can significantly improve the model, both in terms of predicting the experimental ground reaction force and also duplicating the Inverse Kinematics joint angles. Using another muscle force prediction scheme should be top priority in development of future computational models. Knee contact forces in the computational models of Kim et al. (2009) affected the ground reaction force. A more sophisticated muscle force prediction scheme that predicts better muscle forces will predict more accurate knee joint forces, thus predicting the ground reaction forces more accurately.

The proposed computational method permits a better understanding of knee biomechanics without sacrificing the computational cost and time. The main issue identified that would enhance the model prediction is accurate muscle force calculation. When it comes to muscle force predictions, due to the indeterminate nature of the system, there is no confidence on the predicted values. Depending on the optimization technique, different set of results will be predicted for the same boundary conditions. Moreover, direct measurement of the muscle force and joint contact mechanics during ambulatory activities are either non-existent or extremely limited, hindering the possibility of optimization scheme validation. Therefore, the future work should mainly focus on finding a better muscle scheme.

Appendix 1 - Ligament Modeling

This appendix presents an overview of the mechanical properties and also insertion and origin of the ligaments used in this computational study. A summary of ligament bundle stiffness is presented at the end of the chapter.

ACL Characteristics:

The Anterior Cruciate Ligament (ACL) is composed of two separate bundles, the anteromedial bundle (AM) and posterolateral bundle (PL).

The entire ACL is 32 mm long across population with a range of 22-41 mm [Amis et al., 1991]. Anderson et al. (2001) reported a cross section mean value of 42.5 mm^2 in male athletes and 36.1 mm^2 in female athletes for the entire ACL.

ACL arises from the medial aspect of lateral femoral condyle, runs an oblique path and fans out as it is attached to the tibia, lateral and anterior to intercondylar spine [Dienst et al., 2002]. AM bundle originates more proximally and PL bundle originates more distally. On the insertion site, AM inserts anteromedially (hence anteromedial) and PL inserts posterolatrally (hence posterolateral) [Chhabra et al. 2006]. In order to identify the femoral origin, the lateral intercondylar ridge and the lateral bifurcate ridge are used. Just posterior to the lateral intercondylar ridge, origins of two bundles are separated by the lateral bifurcate ridge (An osseous ridge between the origins of two bundles). In order to identify the tibia insertion, medial and lateral intercondylar tubercles were utilized [Forsythe et al. 2010].

Butler et al. (1992) examined the ligamentous restrains of the human knee in the Anterior-Posterior drawer. Tangent Modulus of the ACL bundles was evaluated to be 283±114 in the AM and 154±120 in the PL bundle.

ACL resists the anterior translation of the tibia. ACL is also a secondary stabilizer against internal rotation of the tibia and the valgus moments [Buoncristiani et al. 2006]. Single bundle ACL reconstruction surgeries are usually successful in restoring the anterior-posterior knee stability. But the secondary stabilizing function of the ACL in restraining internal tibial torque combined with valgus torque is not successfully restored [Woo et al. 2002]. However, double bundle ACL reconstruction surgeries restore kinematics of the knee more closely. The two bundles are not isometric; the AM is a primary restraint against anterior tibial loads. However, the PL is a stabilizer near full extension, especially against rotary loads [Peterson et al. 2007].

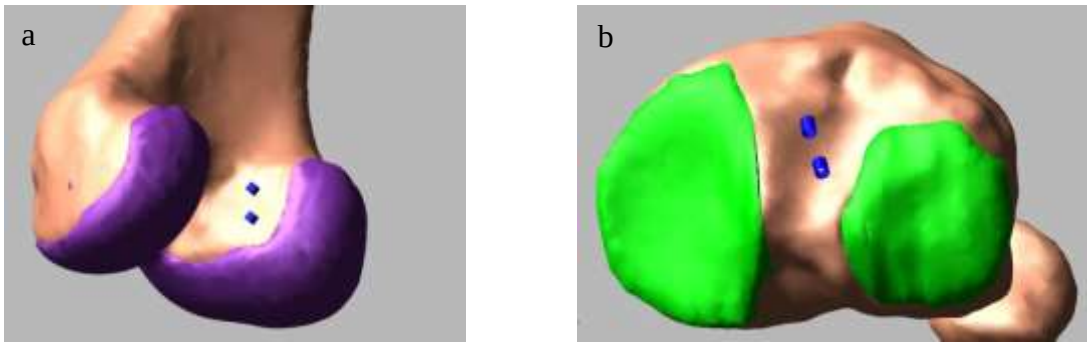

Figure A.1. ACL origin (a) and insertion (b) sites.

PCL Characteristics:

The Posterior Cruciate Ligament (PCL) is also consisted of two bundles; the anterolateral (AL) and the posteromedial (PM). However, the bundles are inseparable.

AL bundle has an average length of 35.5 mm while PM bundle's average length is 38.7 mm. The mean cross sectional area of the AL bundle is 43 mm^2 while PM has a significantly smaller mean cross section of 10 mm^2 [Bowman et al., 2009]. Contrary to ACL, femoral insertion of PCL is larger than its tibial insertion [Harner et al. 1995].

PCL originates from the lateral surface of the medial femoral condyle and attaches to posterior tibia, posterolateral to the ACL insertion. The average femoral footprint of the

AL and PM expands over an area of 118 mm^2 and 90 mm^2 respectively [Lopes et al. 2008] and the average tibial insertion footprint of the AL and PM expands over an area of 93 mm^2 and 151 mm^2 [Tajima et al. 2009].

Harner et al. (1995) studied the PCL mechanical properties and found tangent modulus of AL and PM bundles to be 294±115 and 150±69 MPa respectively.

Resisting posterior translation of the tibia on the femur at all flexion angles is the primary function of the PCL [Gollehon DL et al. 1987]. Moreover, PCL resists to some extent against external rotation of the lower leg and also extreme varus and valgus moments [Grood et al. 1988].

The AL is tight in flexion and mainly resists the posterior load in 70-90 flexion range. PM is tight in extension and resists the posterior loads on the tibia in extension [Harner et al. 1995].

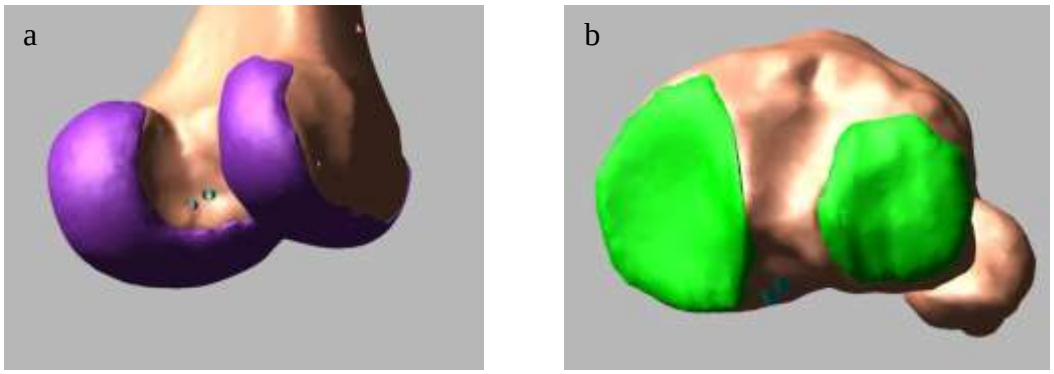

Figure A.2. PCL origin (a) and insertion (b) sites.

ACL and PCL have two bundles that take the load differently and have different biomechanical functionality. However, LCL, Superficial MCL and Deep MCL are more isometric in nature.

MCL Characteristics:

Robinson et al. (2005) studied the passive constraints in the posteromedial aspect of the knee and described three main structures: the deep MCL (dMCL) with longitudinal parallel fibers, superficial MCL (sMCL) with and Posteromedial capsule (PMC).

MCL is approximately 80mm. MCL originates from the medial femoral epicondyle and attaches to the posteromedial margin of the metaphysis of the tibia [Woo et al., 2002]. The femoral origin is 79.7±17.6 mm^2 for SMCL and 71.9±14.8 $mm^2$for DMCL. The tibial insertion is 348.6±42.8 mm^2 and 63.6±13.4 mm^2 for SMCL and DMCL respectively [Liu et al., 2011].

Robinson et al. (2005) examined the properties of each functional unit and found stiffness values for sMCL, dMCL and PMC to be 80±8, 42±14 and 56±20 N/mm respectively.

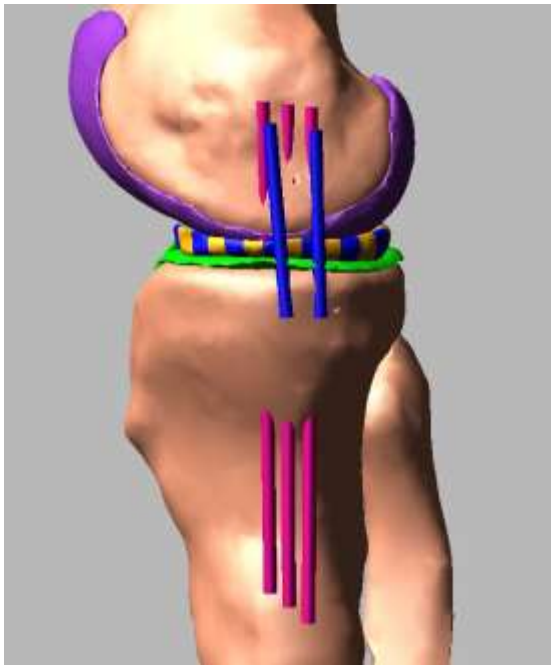

Figure A.3. Superficial (magenta) and Deep (blue) bundles of MCL.

LCL Characteristics:

Lateral Collateral Ligament (LCL) runs from the lateral epicondyle of femur and attach to the top of the fibular head. LCL femoral attachment is located at equal distance from the posterior and distal border of the lateral femoral condyle and the tibial insertion is on a V-shaped plateau on head of the fibula [Brad et al. 2000].

Blankevoort and Huiskes (1991) assigned a value of 2000 N to the stiffness of LCL ligament bundles in a validated three dimensional mathematical model of the knee.

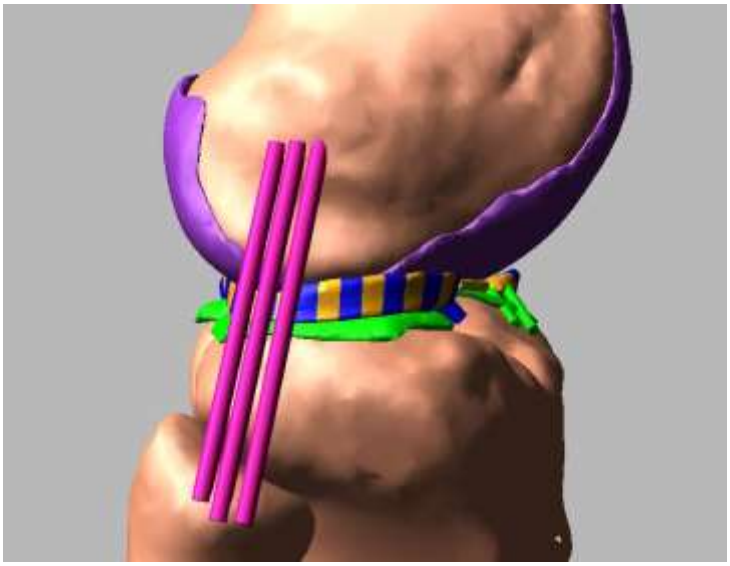

Figure A.4. LCL is modeled as three bundles.

MPFL and LPFL Characteristics:

Medial patellofemoral ligament (MPFL) and lateral patellofemoral ligament (LPFL) play an important role in passive medial-lateral stability of patella. MPFL has been studied extensively because of the prevalence of MPFL complex injuries, but there is not much data available on LPFL.

MPFL is triangle shaped with a length of 59±6.6 mm with a width of 8.8±2.9 mm at the patellar insertion.

MPFL originates from the most prominent edge of patella and inserts into an elliptical area of the femur between medial epicondyle and adductor tubercle with a surface area of 56.5±16.9 mm^2. The center of the area is 10.6±2.5 mm distal to the adductor tubercle on the femur. The wrapping of MPFL and LPFL are not modeled in this project. However, due to the low stiffness of these ligaments, the changes would be insignificant.

A mechanical testing of MPFL showed a tensile strength of 208±90 N at a 26±7mm displacement [Mountney et al. 2005].

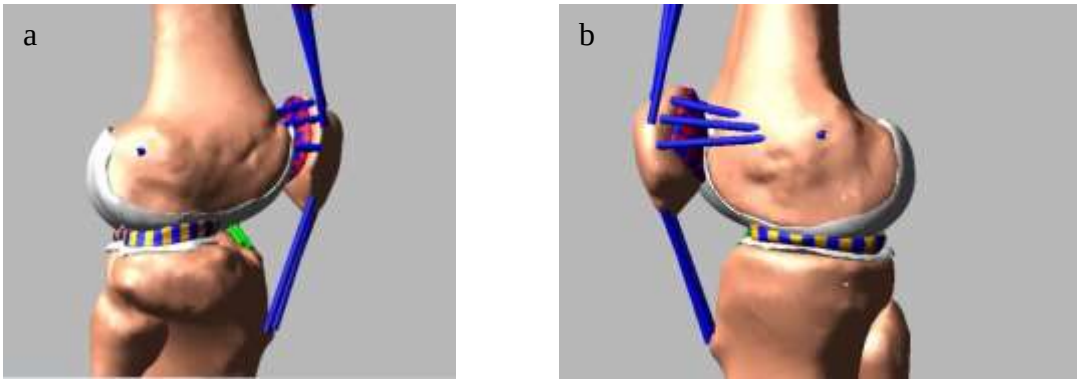

Figure A.5. LPFL (a) and MPFL (b) are modeled as three straight lines.

Patellar Tendon Characteristics:

Hashemi et al. (2005) studied the mechanical and physical properties of patellar tendon and reported a value of 20.68±8.72 mm^2 for cross-sectional area while reporting a length of 50.93±3.78 mm (52.34±3.78mm for male subjects and 49.53±3.76mm for female subjects).

The Elastic modulus was reported to be 501.4±143.6MPa and 513.4±134.1MPa for male and female subjects respectively.

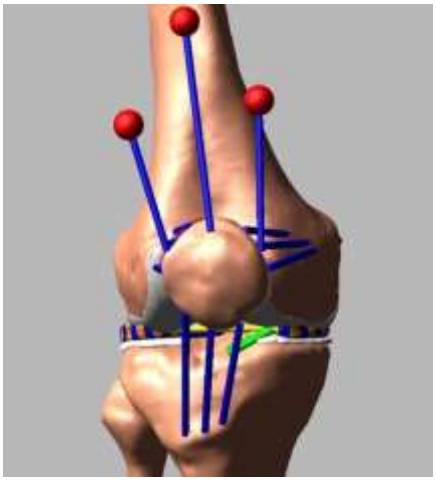

Figure A.6. Patellar Tendon is modeled as three bundles connecting the patella to the tibia.

Meniscal Horn Attachments Characteristics:

Each meniscus is attached to the tibia by short ligaments called Horn attachments. These ligaments run from the ends of each meniscus to small depressions between the condyles of the tibia. Length and cross-sectional area of each horn is presented in Table A.1 [Hauch et al., 2010].

Horn Attachments	Length	Cross-sectional area
Lateral Anterior	13.02±3.230	23.22±5.820
Lateral Posterior	9.795±2.365	21.73±13.17
Medial Anterior	13.87±3.837	18.73±8.470
Medial Posterior	7.170±2555	30.70±7.700

Table A.1. The Dimensions of Horn Attachments.

Medial anterior (MA) horn attachment of meniscus inserts in the anterior intercondylar area and it is mostly distinguished by a tubercle over an area of 139±43 mm^2. The medial posterior (MP) horn is attached next to the PCL behind the medial intercondylar over an area of 80±10 mm^2.

Lateral anterior (LA) horn attachment of the meniscus inserts next to the tibial attachment of ACL over an area of 93±25 mm^2. The lateral posterior (LP) attachment inserts over an area from the medial intercondylar tubercle to the posterior slope of the lateral intercondylar tubercle over an area of 115±51 mm^2 [Kohn and Moreno, 1995].

Linear elastic modulus of for anterior attachments and posterior attachments of meniscus are 169±130 MPa and 90.8±64.9 MPa, respectively.

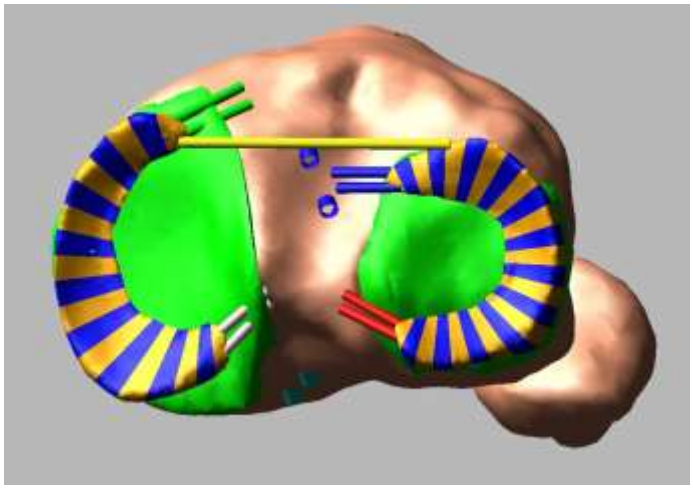

Figure A.7. Each meniscus is attached to the tibia via two anterior and two posterior bundles. The AIML is also modeled between the lateral meniscus and lateral meniscus.

Wrisberg and Humphrey Ligaments:

In addition to ACL and PCL, Some people have two additional ligaments in the knee capsule. Anterior meniscofemoral ligament (MFL) or Humphrey ligament is attached anterior to the PCL. However, posterior MFL or Wrisberg ligament is posterior to the PCL (Girgis et al., 1975). They serve as secondary stabilizers to PCL to serve as posterior tibial translation stabilizer.

These ligaments are not present across the population and they are not included in the models presented in this thesis.

Summary of Stiffness Properties:

The ligament forces in the model were predicted by a piece-wise function (Eq. 2.2.) which requires a set of inputs:

1. The insertion and origin of the ligament bundle in order to calculate the ligament length at each instance.
2. Zero load length of the ligament bundle.
3. Ligament stiffness (k) in Newton [The static portion of the predicted force is calculated by multiplying this stiffness value into a Normalized length (ε)].
4. The length at which the toe region ends was assumed to be 1.06 times the zero-load length of each ligament (ε_1 in equation 2.2 was assumed to be 0.03).
5. Damping coefficient when the muscle is shortening was assumed to be 0.5 Ns/mm
6. Damping coefficient when the muscle is lengthening was assumed to be 0.01 Ns/mm.

In the following, a summary of calculations performed to derive the stiffness of each ligament bundle is presented.

ACL and PCL:

For the ACL and PCL bundles, Modulus of each bundle is presented in the literature [Butler et al., 1992 and Harner et al., 1995]. Anderson et al. (2001) reported a cross sectional area of 36 mm^2 across the female population. The cross sectional area was assumed to be divided between the two bundles. The cross sectional area of the AL-PCL and PM-PCL was reported to be 43 mm^2 and 10 mm^2 respectively by Bowman Jr. and Sekiya (2009). The multiplication of the cross-section into the Modulus of Elasticity will yield the stiffness of each ligament in Newton.

	Modulus of Elasticity (MPa)	Cross Sectional Area (mm^2)	Multiplication	Stiffness (N)
AM-ACL	283	18	5094	5100
PL-ACL	154	18	2772	2800
AL-PCL	294	43	12642	12500
PM-PCL	150	10	1500	1500

Table A.2. Stiffness of the cruciate ligaments is calculated by multiplication of Modulus of Elasticity and Cross Sectional Area.

MCL:

Robinson et al. (2005) reported stiffness of 80 N/mm and 42 N/mm for superficial bundle and Deep bundle of MCL. Therefore each bundle of MCL was assumed to have a stiffness of 26.67 N/mm (80/3). But the stiffness value for the Deep bundle was not divided to the number of ligament bundle. The values were then multiplied to the zero-load-length of each bundle to calculate the stiffness in Newton.

	Stiffness (N/mm)	Length(mm)	Multiplication	Value used in the model
A-SMCL	26.67	95.02	2533.87	2500
I-SMCL	26.67	100.58	2682.13	2600
P-SMCL	26.67	104.04	2774.45	2700
A-DMCL	42	35.73	1500.66	1500
P-DMCL	42	35.44	1488.48	1500

Table A.3. Stiffness of the MCL bundles is calculated by multiplication of Stiffness and Length.

LCL:

The LCL stiffness values were all duplicated from the computational model developed by Blakevoort and Huiskes (1991). They modeled the LCL as 3 bundles each with a stiffness value of 2000 N.

MPFL and LPFL:

Mountney et al. (2005) reported a value of 208 N for tensile strength of MPFL over a 26 mm displacement, thus a 208/26=8 N/mm stiffness was assumed for the whole ligament. This stiffness was divided into three bundles (2.67 N/mm) and then multiplied

by the length ligament bundle of the subject in the MRI. Since there was not data on the stiffness of the LPFL, the stiffness of the MPFL and LPFL were assumed to be equal.

	Stiffness	Length	Multiplication	Stiffness Values (N/mm)
P-MPFL	2.67	62.5	166.67	150
C-MPFL	2.67	59.1	157.60	150
D-MPFL	2.67	60.4	161.07	150
P-LPFL	2.67	61.2	163.20	150
C-LPFL	2.67	58	154.67	150
D-LPFL	2.67	56.1	149.60	150

Table A.4. Stiffness of MPFL and LPFL are calculated by multiplication of Stiffness and Length.

Patellar Tendon:

Hashemi et al. (2005) reported a stiffness value of 513.4 MPa for the patellar tendon and cross sectional area of 20.68 mm^2. This stiffness was divided between three bundles, thus we set the stiffness of each bundle at 513.4*20.68/3=3533.04 N ≈3500.

Appendix 2 – Anthropometric Equations

In 1971, Calspan Corporation (Cheektowaga, New York), a research laboratory for Curtiss-Wright Corporation (Buffalo, New York), developed a three dimensional computer model of human body, Articulated Total Body (ATB), to use in a vehicle crash simulator, Crash Victim Simulator (CVS). The model consisted of fifteen rigid bodies, connected by ball-and-socket and hinge joints in parallel with torsional springs.

CVS required the geometry and inertial properties of each body part, thus, requiring the user to input mass, inertia and center of mass location for each body segment as well as location of each joint center. In order to automate the process of inputting these variables, the company developed the GOOD (Generator Of Body Data) software which was later updated to GEBOD (GEnerator of BODy Data) software. GEBOD IV, an interactive menu driven program, is the latest version and this Appendix discusses the regression equations incorporated in the software.

In the ATB model, each body segment is represented with an ellipsoid. The dimensions of the segment and the center of joint location are defined based on the size and location of the corresponding ellipsoid.

There are four set of first-order linear regression equations based on the height or/and weight of the subject that have been derived from body measurement survey data or sterophotometric data:

1. Body Measurements
2. Joint Locations
3. Segment Volumes(which is used to calculate the mass of each segement)
4. Segment Principle Moments of Inertia

These equations have been derived from body measurement survey data or sterophotometric data.

The female equation set is based on the anthropometric works of Clauser et al. (1972) on Air Force women and the stereophotometric works of Young et al. (1983).

The male equation set is based on the anthropometric works of Grunhofer and Kroh (1975) on German an USA Air Force flying personnel and the stereophotometric works of McConville et al. (1980).

GEBOD generates the data based on height or/and weight of the subject. Using the survey regression equations, 32 body dimensions are created which are later used in geometric equations to create the ellipsoids representing the body segments. Using the Stereophtometric regression equations, Mass properties and also joint Locations are created.

For each of these 32 body measurements, three regression equations are presented, one based on the height, one based on the weight and one based on both height and weight of the subject and as expected the last one is the most accurate one. Therefore in our macros, the equations in which both the height and weight have been incorporated are used. For Example;

Female Ankle circumference = (0.1720e-1)*BodyWeight + (0.1177e-1)*BodyHeight*+5.361

It should be noted that the regression equations are presented in English units, thus the Ankle circumference in mm is equal to:

Female Ankle Circumference= (((0.1720e-1)*BodyWeight*2.204623
+ (0.1177e-1)*BodyHeight*0.03937
+ 5.361)
* 25.4)

References

Adams JG, McAlindon T, Dimasi M, Carey J, Eustace S. (1999) "Contribution of meniscal extrusion and cartilage loss to joint space narrowing in osteoarthritis." Clin Radiol; 54(8):502-6.

AHA Statistical Update - Heart Disease and Stroke Statistics (2014 Update) A Report From the American Heart Association.

Amis AA, Dawkins GP. (1991) "Functional anatomy of the anterior cruciate ligament. Fibre bundle actions related to ligament replacements and injuries." J Bone Joint Surg Br; 73(2):260-7.

Anderson AF, Dome DC, Gautam S, Awh MH, Rennirt GW. (2001) "Correlation of anthropometric measurements, strength, anterior cruciate ligament size, and intercondylar notch characteristics to sex differences in anterior cruciate ligament tear rates." Am J Sports Med; 29(1):58-66.

Andriacchi TP, Mündermann A, Smith RL, Alexander EJ, Dyrby CO, Koo S. (2004) "A framework for the in vivo pathomechanics of osteoarthritis at the knee." Ann Biomed Eng; 32(3):447-57.

Arnold, E. M., Ward, S. R., Lieber, R. L. and Delp, S. L. (2010) "A model of the lower limb for analysis of human movement." Ann. Biomed. Eng; 38, 269-279.

Baldwin, M. A., Laz, P. J., Stowe, J. Q., & Rullkoetter, P. J. (2009) "Efficient probabilistic representation of tibiofemoral soft tissue constraint." Comput Methods Biomech Biomed Engin; 12(6), 651-659. doi: 10.1080/10255840902822550

Bei Y, Fregly BJ (2004) "Multibody dynamic simulation of knee contact mechanics" Medical Engineering & Physics; 26(9):777–789.

Bertozzi, L., Stagni, R., Fantozzi, S., & Cappello, A. (2007) "Knee model sensitivity to cruciate ligaments parameters: a stability simulation study for a living subject." J Biomech, 40 Suppl 1, S38-44. doi: 10.1016/j.jbiomech.2007.02.018

Besier TF, Gold GE, Beaupré GS, Delp SL. (2005) "A modeling framework to estimate patellofemoral joint cartilage stress in vivo." Med Sci Sports Exerc; 37(11):1924-30.

Blankevoort L, Huiskes R. (1991) "Ligament-bone interaction in a three-dimensional model of the knee." J Biomech Eng; 113(3):263-9.

Blankevoort L1, Huiskes R, de Lange A. (1991) "Recruitment of knee joint ligaments." J Biomech Eng; 113(1):94-103.

Bowman Jr KF, Sekiya JK. (2009) "Anatomy and Biomechanics of the Posterior Cruciate Ligament and Other Ligaments of the Knee." Operative Techniques in Sports Medicine; 17:126–134.

Brindle T, Nyland J, Johnson DL. (2001) "The meniscus: review of basic principles with application to surgery and rehabilitation." J Athl Train; 36(2):160-9.

Brophy RH, Wright RW, Matava MJ. (2009) "Cost analysis of converting from single-bundle to double-bundle anterior cruciate ligament reconstruction." Am J Sports Med; 37(4):683-7. doi: 10.1177/0363546508328121. Epub 2009 Feb 9.

Bruns K, Svensson F, Turkiewicz A, Wirth W, Guermazi A, Eckstein F, Englund M. "Meniscus body position and its change over four years in asymptomatic adults: a cohort study using data from the Osteoarthritis Initiative (OAI)." BMC Musculoskelet Disord; 15:32. doi: 10.1186/1471-2474-15-32.

Buoncristiani AM, Tjoumakaris FP, Starman JS, Ferretti M, Fu FH. (2006) "Anatomic double-bundle anterior cruciate ligament reconstruction." Arthroscopy; 22(9):1000-6.

Butler DL, Guan Y, Kay MD, Cummings JF, Feder SM, Levy MS. (1992) "Location-dependent variations in the material properties of the anterior cruciate ligament." J Biomech; 25(5):511-8.

Chandoran KB (1992). "Cardiovascular Biomechanics" New York University Biomedical Engineering Series

Chhabra A, Starman JS, Ferretti M, Vidal AF, Zantop T, Fu FH. (2006)" Anatomic, radiographic, biomechanical, and kinematic evaluation of the anterior cruciate ligament and its two functional bundles." J Bone Joint Surg Am; 88 Suppl 4:2-10.

Costa C.R., Morrison W.B., Carrino J.A. (2004) "Medial meniscal extrusion on knee MRI: is extent associated with severity of degeneration or type of tear?" AJR Am J Roentgenol 183: 17–23

Couppé C, Hansen P, Kongsgaard M, Kovanen V, Suetta C, Aagaard P, Kjaer M, Magnusson SP. (2009) "Mechanical properties and collagen cross-linking of the patellar tendon in old and young men." J Appl Physiol; 107(3):880-6. doi: 10.1152/japplphysiol.00291.2009. Epub 2009 Jun 25.

D'Agata SD, Pearsall AW 4th, Reider B, Draganich LF. (1993) "An in vitro analysis of patellofemoral contact areas and pressures following procurement of the central one-third patellar tendon." Am J Sports Med; 21(2):212-9.

Danso EK, Mäkelä JT, Tanska P, Mononen ME, Honkanen JT, Jurvelin JS, Töyräs J, Julkunen P, Korhonen RK. (2015) "Characterization of site-specific biomechanical properties of human meniscus-Importance of collagen and fluid on mechanical nonlinearities." J Biomech; 48(8):1499-507. doi: 10.1016/j.jbiomech.2015.01.048. Epub 2015 Feb 7.

DeFrate LE, Gill TJ, Li G. (2004) "In vivo function of the posterior cruciate ligament during weight bearing knee flexion." Am J Sports Med; 32:1923-1928. Epub 2004/12/02.

Delp SL, Loan JP, Hoy MG, Zajac FE, Topp EL, Rosen JM. (1990) "An interactive graphics-based model of the lower extremity to study orthopaedic surgical procedures." IEEE Trans Biomed Eng; 37(8):757-67.

Devereaux M.D. and S. M. Lachmann (1983) "Athletes attending a sports injury clinic - A review." Br J Sports Med; 17(4): 137–142.

De Luca CJ, Forrest WJ (1972) "An Electrode for Recording Single Motor Unit Activity During Strong Muscle Contractions." IEEE TRANSACTIONS ON BIOMEDICAL ENGINEERING, VOL. BME-19, NO. 5

Dienst M, Burks RT, Greis PE. (2002) “Anatomy and biomechanics of the anterior cruciate ligament.” Orthop Clin North Am; 33(4):605-20, v.

Donahue TL, Fisher MB, A Maher S. (2015) “Meniscus mechanics and mechanobiology.” J Biomech; 48(8):1341-2. doi: 10.1016/j.jbiomech.2015.03.020. Epub 2015 Mar 30.

Donahue TL, Hull ML, Rashid MM, Jacobs CR (2002) “A finite element model of the human knee joint for the study of tibio-femoral contact” J Biomech Eng; 124(3):273-80.

Duthon VB, Barea C, Abrassart S, Fasel JH, Fritschy D, Ménétrey J. (2006) “Anatomy of the anterior cruciate ligament.” Knee Surg Sports Traumatol Arthrosc; 14(3):204-13. Epub 2005 Oct 19.

Englund M, Roos EM, Lohmander LS (2003) “Impact of type of meniscal tear on radiographic and symptomatic knee osteoarthritis: A sixteen-year follow-up of meniscectomy with matched controls” Arthritis Rheum; 48(8):2178-87.

Fang Liu, Bing Yue, Hemanth R Gadikota, Michal Kozanek, Wanjun Liu, Thomas J Gill, Harry E Rubash, and Guoan Li. (2010) “Morphology of the medial collateral ligament of the knee” J Orthop Surg Res; 5: 69. Published online 2010 Sep 16. doi: 10.1186/1749-799X-5-69

Forsythe B, Kopf S, Wong AK, Martins CA, Anderst W, Tashman S, Fu FH. (2010) “The location of femoral and tibial tunnels in anatomic double-bundle anterior cruciate ligament reconstruction analyzed by three-dimensional computed tomography models.” J Bone Joint Surg Am; 92(6):1418-26. doi: 10.2106/JBJS.I.00654.

Fulkerson JP, Shea KP. (1990) “Disorders of patellofemoral alignment.” J Bone Joint Surg Am; 72(9):1424-9.

Gallagher S, Heberger JR (2013) "Examining the Interaction of Force and Repetition on Musculoskeletal Disorder Risk A Systematic Literature Review". Hum Factors; 55(1):108-24.

Gelber AC, Hochberg MC, Mead LA, Wang NY, Wigley FM, Klag MJ (2000) “Joint injury in young adults and risk for subsequent knee and hip osteoarthritis.” Ann Intern Med; 133(5):321-8.

Girgis FG, Marshall JL, Monajem A. (1975) "The cruciate ligaments of the knee joint. Anatomical, functional and experimental analysis." Clin Orthop Relat Res; (106):216-31.

Gollehon DL, Torzilli PA, Warren RF. (1987) "The role of the posterolateral and cruciate ligaments in the stability of the human knee. A biomechanical study." J Bone Joint Surg Am; 69(2):233-42.

Goudakos IG, König C, Schöttle PB, Taylor WR, Hoffmann JE, Pöpplau BM, Singh NB, Duda GN, Heller MO. (2010) "Regulation of the patellofemoral contact area: an essential mechanism in patellofemoral joint mechanics?" J Biomech; 43(16):3237-9. doi: 10.1016/j.jbiomech.2010.07.029. Epub 2010 Aug 13.

Grood ES, Stowers SF, Noyes FR. (1988) "Limits of movement in the human knee. Effect of sectioning the posterior cruciate ligament and posterolateral structures." J Bone Joint Surg Am; 70(1):88-97.

Grood ES, Suntay WJ. (1983) "A joint coordinate system for the clinical description of three-dimensional motions: application to the knee." J Biomech Eng; 105(2):136-44.

Guess TM, Liu H, Bhashyam S, Thiagarajan G. (2013) "A multibody knee model with discrete cartilage prediction of tibio-femoral contact mechanics." Comput Methods Biomech Biomed Engin; 16(3):256-70. doi: 10.1080/10255842.2011.617004. Epub 2011 Oct 4.

Guess TM, Stylianou AP, and Kia M. (2014) "Concurrent Prediction of Muscle and Tibiofemoral Contact Forces During Treadmill Gait" J Biomech Eng; 136(2): 0210321–0210329. Published online 2014 Feb 5. doi: 10.1115/1.4026359

Guess TM, Thiagarajan G, Kia M, Mishra M. (2010) "A subject specific multibody model of the knee with menisci." Med Eng Phys; 32(5):505-15. doi: 10.1016/j.medengphy.2010.02.020. Epub 2010 Mar 31.

Harner CD, Xerogeanes JW, Livesay GA, Carlin GJ, Smith BA, Kusayama T, Kashiwaguchi S, Woo SL. (1995) "The human posterior cruciate ligament complex: an interdisciplinary study. Ligament morphology and biomechanical evaluation." Am J Sports Med; 23(6):736-45.

Hartshorn T, Otarodifard K, White EA, Hatch GF 3rd. 2013. Radiographic landmarks for locating the femoral origin of the superficial medial collateral ligament. Am J Sports Med; 41(11):2527-32. doi: 10.1177/0363546513504895. Epub 2013 Oct 3.

Hashemi J, Chandrashekar N, Slauterbeck J. (2005) "The mechanical properties of the human patellar tendon are correlated to its mass density and are independent of sex." Clin Biomech (Bristol, Avon); 20(6):645-52. Epub 2005 Mar 29.

Hauch K. N., Villegas D. F., Haut Donahue T. L. (2010) "Geometry, time-dependent and failure properties of human meniscal attachments." J Biomech; 43(3):463–8.

Haut Donahue TL, Hull ML, Rashid MM, Jacobs CR. (2003) "How the stiffness of meniscal attachments and meniscal material properties affect tibio-femoral contact pressure computed using a validated finite element model of the human knee joint." J Biomech; 36(1):19-34.

Helmick CG, Felson DT, Lawrence RC, Gabriel S, Hirsch R, Kwoh CK, Liang MH, Kremers HM, Mayes MD, Merkel PA, Pillemer SR, Reveille JD, Stone JH; National Arthritis Data Workgroup. (2008) "Estimates of the Prevalence of Arthritis and Other Rheumatic Conditions in the United States" Arthritis Rheum; 58(1):15-25.

Hewett TE, Myer GD, Ford KR, Heidt RS Jr, Colosimo AJ, McLean SG, van den Bogert AJ, Paterno MV, Succop P. (2005) "Biomechanical measures of neuromuscular control and valgus loading of the knee predict anterior cruciate ligament injury risk in female athletes: a prospective study." Am J Sports Med; 33(4):492-501. Epub 2005 Feb 8.

Heyse TJ, Tucker SM, Rajak Y, Kia M, Lipman JD, Imhauser CW, Westrich GH (2015) "Frontal plane stability following UKA in a biomechanical study" Arch Orthop Trauma Surg; [Epub ahead of print]

Huberti HH, Hayes WC. (1984) "Patellofemoral contact pressures. The influence of q-angle and tendofemoral contact." J Bone Joint Surg Am; 66(5):715-24.

Hunter D.J., Zhang Y.Q., Niu J.B., Tu X., Amin S., Clancy M. (2006) "The association of meniscal pathologic changes with cartilage loss in symptomatic knee osteoarthritis." Arthritis Rheum; 54: 795–801

Imhauser C, Mauro C, Choi D, Rosenberg E, Mathew S, Nguyen J, Ma Y, Wickiewicz T (2013) "Abnormal Tibiofemoral Contact Stress and Its Association With Altered Kinematics After Center-Center Anterior Cruciate Ligament Reconstruction." Am J Sports Med; 41(4):815-25.

Isman RE, Inman VT. (1969) "Anthropometric studies of the human foot and ankle." Bull Pros Res; 10–11:97–129

Kanamori A, Woo SL, Ma CB, Zeminski J, Rudy TW, Li G, Livesay GA (2000) "The forces in the anterior cruciate ligament and knee kinematics during a simulated pivot shift test: A human cadaveric study using robotic technology" Arthroscopy; 16(6):633-9.

Kiapour AM, Kaul V, Kiapour A, Quatman CE, Wordeman SC, Hewett TE, Demetropoulos CK, Goel VK (2014) "The Effect of Ligament Modeling Technique on Knee Joint Kinematics: A Finite Element Study" Appl Math (Irvine); 4(5A):91-97.

Kim HJ, Fernandez JW, Akbarshahi M, Walter JP, Fregly BJ, Pandy MG. (2009) "Evaluation of predicted knee-joint muscle forces during gait using an instrumented knee implant." J Orthop Res; 27(10):1326-31. doi: 10.1002/jor.20876.

Kanamori A, Woo SL, Ma CB, Zeminski J, Rudy TW, Li G, Livesay GA (2000) "The Forces in the Anterior Cruciate Ligament and Knee Kinematics During a Simulated Pivot Shift Test: A Human Cadaveric Study Using Robotic Technology" Arthroscopy; 16(6):633-9.

Kohn D, Moreno B. Meniscus insertion anatomy as a basis for meniscus replacement: a morphological cadaveric study. Arthroscopy; 11(1):96–103

Lai Y, Chen W, Huang C, Cheng C, Chan K, and Chang T (2015) "The Effect of Graft Strength on Knee Laxity and Graft In-Situ Forces after Posterior Cruciate Ligament Reconstruction" PLoS One; 10(5): e0127293.

LaPrade RF, Engebretsen AH, Ly TV, Johansen S, Wentorf FA, Engebretsen L. (2007) "The anatomy of the medial part of the knee." J Bone Joint Surg Am; 89(9):2000-10.

Lee S, Seong SC, Jo H, Park YK, Lee MC (2004) "Outcome of anterior cruciate ligament reconstruction using quadriceps tendon autograft" Arthroscopy; 20(8):795-802.

Lopes OV Jr, Ferretti M, Shen W, Ekdahl M, Smolinski P, Fu FH. (2008) "Topography of the femoral attachment of the posterior cruciate ligament." J Bone Joint Surg Am; 90(2):249-55. doi: 10.2106/JBJS.G.00448.

Li G., Gil J., Kanamori A., Woo S. L. (1999). "A validated three-dimensional computational model of a human knee joint." J Biomech Eng; 121(6), 657-662.

Li G., Gill T. J., DeFrate L. E., Zayontz S., Glatt V., Zarins B. (2002) "Biomechanical consequences of PCL deficiency in the knee under simulated muscle loads--an in vitro experimental study." J Orthop Res; 20(4), 887-892. doi: 10.1016/S0736-0266(01)00184-X.

Li G, Lopez O, Rubash H. (2001) "Variability of a three-dimensional finite element model constructed using magnetic resonance images of a knee for joint contact stress analysis." J Biomech Eng; 123(4):341-6.

Li L, Tong K, Song R, Koo TK. (2007) "Is maximum isometric muscle stress the same among prime elbow flexors?" Clin Biomech (Bristol, Avon); 22(8):874-83. Epub 2007 Aug 2.

Lin YC, Walter JP, Banks SA, Pandy MG, Fregly BJ. (2010) "Simultaneous prediction of muscle and contact forces in the knee during gait." J Biomech; 43(5):945-52. doi: 10.1016/j.jbiomech.2009.10.048. Epub 2009 Dec 5.

Liu F, Gadikota HR, Kozánek M, Hosseini A, Yue B, Gill TJ, Rubash HE, Li G. (2011) "In vivo length patterns of the medial collateral ligament during the stance phase of gait." Knee Surg Sports Traumatol Arthrosc; 19(5):719-27. doi: 10.1007/s00167-010-1336-5. Epub 2010 Dec 11.

Meister BR, Michael SP, Moyer RA, Kelly JD, Schneck CD. (2000) "Anatomy and kinematics of the lateral collateral ligament of the knee." Am J Sports Med; 28(6):869-78.

Meyer SA, Brown TD, Pedersen DR, Albright JP. (1997) "Retropatellar contact stress in simulated patella infera." Am J Knee Surg; 10(3):129-38.

Mootanah R, Imhauser CW, Reisse F, Carpanen D, Walker RW, Koff MF, Lenhoff MW, Rozbruch SR, Fragomen AT, Dewan Z, Kirane YM, Cheah K, Dowell JK, Hillstrom HJ. (2014) "Development and validation of a computational model of the knee joint for the evaluation of surgical treatments for osteoarthritis." Comput Methods Biomech Biomed Engin; 17(13):1502-17. doi: 10.1080/10255842.2014.899588. Epub 2014 May 1.

Mountney J, Senavongse W, Amis AA, Thomas NP. (2005) "Tensile strength of the medial patellofemoral ligament before and after repair or reconstruction." J Bone Joint Surg Br; 87(1):36-40.

Murphy L, Helmick CG (2012) "The impact of osteoarthritis in the United States: a population-health perspective." Am J Nurs; 31(2):85-91.

Nester C, Jones RK, Liu A, Howard D, Lundberg A, Arndt A, Lundgren P, Stacoff A, Wolf P. (2007) "Foot kinematics during walking measured using bone and surface mounted markers." J Biomech; 40(15):3412-23. Epub 2007 Jul 16.

Nigg B. M., Macintosh B. R., and Mester J. (2000) "Biomechanics and Biology of Movement" Human Kinetics, Champaign, IL.

Osti M, Tschann P, Künzel KH, Benedetto KP. (2012) "Anatomic characteristics and radiographic references of the anterolateral and posteromedial bundles of the posterior cruciate ligament." Am J Sports Med; 40(7):1558-63. doi: 10.1177/0363546512445166. Epub 04/26/2012.

Park SE, DeFrate LE, Suggs JF, Gill TJ, Rubash HE, Li G. (2005) "The change in length of the medial and lateral collateral ligaments during in vivo knee flexion." Knee; 12(5):377-82.

Peña E, Calvo B, Martínez MA, Doblaré (2006) "M.A three-dimensional finite element analysis of the combined behavior of ligaments and menisci in the healthy human knee joint." J Biomech; 39(9):1686-701

Peterson RK, Shelton WR, Bomboy AL. (2001) "Allograft versus autograft patellar tendon anterior cruciate ligament reconstruction: A 5-year follow-up." Arthroscopy; 17(1):9-13.

Poh SY, Yew KS, Wong PL, Koh SB, Chia SL, Fook-Chong S, Howe TS. (2012) "Role of the anterior intermeniscal ligament in tibiofemoral contact mechanics during axial joint loading." Knee; 19(2):135-9. doi: 10.1016/j.knee.2010.12.008. Epub 2011 Jan 22.

Raychoudhury S, Hu D, Ren L. (2014) " Three-Dimensional Kinematics of the Human Metatarsophalangeal Joint during Level Walking" Front Bioeng Biotechnol; 2: 73. Published online 2014 Dec 15. doi: 10.3389/fbioe.2014.00073

Robinson JR, Bull AM, Amis AA. (2005) "Structural properties of the medial collateral ligament complex of the human knee." J Biomech; 38(5):1067-74.

Robinson JR, Bull AM, Thomas RR, Amis AA. (2006) "The role of the medial collateral ligament and posteromedial capsule in controlling knee laxity." Am J Sports Med; 34(11):1815-23. Epub 2006 Jun 30.

Seitz AM, Lubomierski A, Friemert B, Ignatius A, Dürselen L. (2012) "Effect of partial meniscectomy at the medial posterior horn on tibiofemoral contact mechanics and meniscal hoop strains in human knees." J Orthop Res; 30(6):934-42. doi: 10.1002/jor.22010. Epub 2011 Nov 9.

Senavongse W, Amis AA. (2005) "The effects of articular, retinacular, or muscular deficiencies on patellofemoral joint stability: a biomechanical study in vitro" J Bone Joint Surg Br.; 87(4):577-82.

Sharf I, and Zhang Y. (2006) "A contact force solution for non-colliding contact dynamics simulation." Multibody Syst Dyn; 16(3):263–90.

Shelburne KB, Torry MR, Pandy MG (2006) "Contributions of muscles, ligaments, and the ground-reaction force to tibiofemoral joint loading during normal gait" J Orthop Res; 24(10):1983-90.

Shim VB, Besier TF, Lloyd DG, Mithraratne K, Fernandez JF. (2015) "The influence and biomechanical role of cartilage split line pattern on tibiofemoral cartilage stress distribution during the stance phase of gait." Biomech Model Mechanobiol.

Stehling C, Souza RB, Hellio Le Graverand MP, Wyman BT, Li X, Majumdar S, Link TM. (2012) "Loading of the knee during 3.0T MRI is associated with significantly increased medial meniscus extrusion in mild and moderate osteoarthritis." Eur J Radiol; 81(8):1839-45. doi: 10.1016/j.ejrad.2011.05.027.

Stein G, Koebke J, Faymonville C, Dargel J, Müller LP, Schiffer G. (2011) "The relationship between the medial collateral ligament and the medial meniscus: a topographical and biomechanical study." Surg Radiol Anat; 33(9):763-6. doi: 10.1007/s00276-011-0814-x. Epub 2011 Apr 19.

Strehl A, Eggli S (2007) "The value of conservative treatment in ruptures of the anterior cruciate ligament (ACL)" J Trauma; 62(5):1159-62.

Tajima G, Nozaki M, Iriuchishima T, Ingham SJ, Shen W, Smolinski P, Fu FH. (2009) "Morphology of the tibial insertion of the posterior cruciate ligament." J Bone Joint Surg Am; 91(4):859-66. doi: 10.2106/JBJS.H.00991.

Tapper EM, Hoover NW. (1969) "Late Results after Meniscectomy" J Bone Joint Surg Am; 51 (3): 517 -603.

Upadhyay N, Vollans SR, Seedhom BB, Soames RW. (2005) "Effect of patellar tendon shortening on tracking of the patella." Am J Sports Med; 33(10):1565-74. Epub 2005 Jul 11.

Wagner HJ. (1976) "Architecture of collagen fibers in the meniscus of the human knee joint, with special reference to the medial meniscus and its connection to the articular ligaments" Z Mikrosk Anat Forsch; 90(2):302-24.

Ward SR, Kim CW, Eng CM, Gottschalk LJ 4th, Tomiya A, Garfin SR, Lieber RL. (2009) "Architectural analysis and intraoperative measurements demonstrate the unique design of the multifidus muscle for lumbar spine stability." J Bone Joint Surg Am; 91(1):176-85. doi: 10.2106/JBJS.G.01311.

Ward SR, Powers CM. (2004) "The influence of patella alta on patellofemoral joint stress during normal and fast walking." Clin Biomech (Bristol, Avon); 19(10):1040-7.

Weiss JA, Gardiner JC, Ellis BJ, Lujan TJ, Phatak NS. (2005) "Three-dimensional finite element modeling of ligaments: technical aspects." Med Eng Phys; 27(10):845-61. Epub 2005 Aug 8.

Wenger A, Wirth W, Hudelmaier M, Noebauer-Huhmann I, Trattnig S, Bloecker K, Frobell RB, Kwoh CK, Eckstein F, Englund M. (2013) "Meniscus body position, size, and shape in persons with and persons without radiographic knee osteoarthritis: quantitative analyses of knee magnetic resonance images from the osteoarthritis initiative." Arthritis Rheum; 65(7):1804-11. doi: 10.1002/art.37947.

Wilmes et al., 2008. Wilmes P., Anagnostakos K., Weth C., Kohn D., and Seil R.: The reproducibility of radiographic measurement of medial meniscus horn position. Arthroscopy 2008; 24: pp. 660-668

Wilmes et al., 2007. Wilmes P., Pape D., Kohn D., and Seil R.: The reproducibility of radiographic measurement of lateral meniscus horn position. Arthroscopy 2007; 23: pp. 1079-1086

Wismans J, Veldpaus F, Janssen J, Huson A, and Struben P. (1980). "A three-dimensional mathematical model of the knee-joint." J Biomech 13(8):677–85.

Woo SL, Debski RE, Withrow JD, Janaushek MA. (1999) "Biomechanics of knee ligaments." Am J Sports Med; 27(4):533-43.

Woo SL, Kanamori A, Zeminski J, Yagi M, Papageorgiou C, Fu FH. (2002) "The effectiveness of reconstruction of the anterior cruciate ligament with hamstrings and patellar tendon . A cadaveric study comparing anterior tibial and rotational loads." J Bone Joint Surg Am; 84-A(6):907-14 .

Wünschel M1, Leichtle U, Lo J, Wülker N, Müller O. (2012) "Differences in tibiofemoral kinematics between the unloaded robotic passive path and a weightbearing knee simulator." Orthop Rev (Pavia); 4(1):e2. doi: 10.4081/or.2012.e2. Epub 2012 Jan 3.

Yang, N. H., Canavan, P. K., Nayeb-Hashemi, H., Najafi, B., & Vaziri, A. (2010) "Protocol for constructing subject-specific biomechanical models of knee joint." Comput Methods Biomech Biomed Engin; 13(5), 589-603. doi: 922674995 [pii]10.1080/10255840903389989.